1864-17

Ninth Workshop on Non-linear Dynamics and Earthquake Predictions

1 - 13 October 2007

Formation and evolution of a population of strike-slip faults in a multiscale cellular automaton model

Clement Narteau

Equipe de Geomorphologie
Laboratoire de Dynamique des Fluides Geologiques
Institut de Physique du Globe de Paris, France

Formation and evolution of a population of strike-slip faults in a multiscale cellular automaton model

Clément Narteau

Laboratoire de Dynamique des Systèmes Géologiques, Institut de Physique du Globe de Paris, 4, *Place Jussieu, Paris, Cedex* 05, 75252, *France.*
E-mail: narteau@ipgp.jussieu.fr

SUMMARY

This paper describes a new model of rupture designed to reproduce structural patterns observed in the formation and evolution of a population of strike-slip faults. This model is a multiscale cellular automaton with two states. A stable state is associated with an 'intact' zone in which the fracturing process is confined to a smaller length scale. An active state is associated with an actively slipping fault. At the smallest length scale of a fault segment, transition rates from one state to another are determined with respect to the magnitude of the local strain rate and a time-dependent stochastic process. At increasingly larger length scales, healing and faulting are described according to geometric rules of fault interaction based on fracture mechanics. A redistribution of the strain rates in the neighbourhood of active faults at all length scales ensures that long range interactions and non-linear feedback processes are incorporated in the fault growth mechanism. Typical patterns of development of a population of faults are presented and show nucleation, growth, branching, interaction and coalescence. The geometries of the fault populations spontaneously converge to a configuration in which strain is concentrated on a dominant fault. In these numerical simulations, the material properties are uniform, so the entire process of fault development arises spontaneously from the pattern of interactions between the elements of the system over time. Furthermore, homogenization of the strain rate along faults and structural regularization of the fault trace can be quantified by analysis of the output patterns. The time dependent stochastic process allows relocation of faults by branching from bends and irregularities of the fault traces. This relocation mechanism involves partitioning of the strain and competition between faults. Possible relationships between the seismic regime and the geometry of the fault population suggest that the fault system may be attracted by a critical point. Towards this critical point, the correlation length (i.e. the length of the largest fault) increases, the proportion of large event is higher and larger faults are able to slip at lower stresses.

Key words: earthquakes, fault slip, faulting, rock fracture, seismotectonics.

GJI Seismology

1 INTRODUCTION

In the upper crust, an important part of the deformation occurs along fault zones via earthquakes or creep. These narrow zones of mechanical failure are surrounded by regions free of significant seismicity. Under the large scale loading system generated by plate tectonics, such a localization of the deformation in space and time implies significant stress transfer. The underlying stress exchange mechanisms are difficult to identify because they vary on a wide range of temporal scales depending on the visco-elastic properties of the upper crust, the creation of new faults and the repetition of earthquakes along them. In addition, stress is difficult to measure in situ, and geophysicists have concentrated more on the determination of strain rates along faults using methods such as geodesy, paleomagnetism and carbon dating. For example, progress in dating technology has enabled geologists to estimate average slip-rates along active faults during the past 10^4 to 10^5 yr (Van der Woerd *et al.* 2000), and paleoseismological studies indicate sequences of large earthquakes in the past 10^2–10^4 yr (Rockwell *et al.* 2000). Furthermore, various analytical and empirical relationships have been proposed to link different morphological properties of active normal faults. For example, the maximum displacement on faults has been related to the length of the fault (see Cowie & Scholz 1992b; Schlische *et al.* 1996; Clark & Cox 1996, for a discussion of the data obtained by different workers), but also to the relative location of the fault trace with respect to the centre of the fault (Gupta & Scholz 2000) and to fault segment interactions during the formation process (Peacock & Sanderson 1991). Thus, in addition to the seismic

catalogues, paleoseismic and geological analysis of active faults as well as geodetic measurements of coseismic and interseismic strain enable geophysicists to constrain faulting processes.

This paper presents a model of rupture whose outputs can be compared with various aspects of the structural patterns observed in the formation and evolution of a population of strike-slip faults. This work forms the second step (i.e. tectonic part) towards a general model of the spatial and temporal structures associated with the earthquake phenomena. The first step (i.e. seismological part) is developed in Narteau (2006) and consists of a detailed description of the temporal properties of the seismicity observed in a model of a single in-plane fault zone. In this model, a hierarchy is imposed and cells of different length scales represent blocks of rock of different dimensions (Narteau *et al.* 2000). Earthquakes are considered as critical phenomena that occur when fractured domains organize themselves at all length scales. Practically, a real-space renormalization technique is applied to the rupture problem (Kadanoff 1966; Reynolds *et al.* 1977; Allègre *et al.* 1982). From the distribution of the broken cells at the microscopic length scale, the state of fracturing is obtained at increasingly larger length scales by applying a geometric failure criterion to independent 2×2 lattices of cells. In a hierarchical system, the implementation of this failure criterion is described as an inverse cascade of fracturing and healing (i.e. transfer of the state of fracturing from smaller to larger length scales). When elements fail at larger length scale the redistribution of the stress in their neighbourhoods applies not only at the macroscopic length scale, but also at the microscopic length scale. Because the cascade of fracturing implies failures at all intermediate length scales, the redistribution mechanism is described as a direct cascade of stress redistribution (i.e. transfer of the stress from larger to smaller length scales). The multiscale cellular automaton presented here retains similar cascade mechanisms, but differs from the model of seismicity in several important respects for the problem of fracture growth.

In Narteau (2006), the loading is constant and external perturbations are only discussed from a conceptual point of view in terms of instantaneous and finite stress variations. In natural data, there is a growing body of evidence that indicates that neighbouring faults interact and that fracturing processes at every length scale are strongly dependent on the interrelated evolution of pre-existing faults. This evidence, coupled with the geomorphological observations of active tectonic regions, reveals that only a model consisting of a set of interacting faults can integrate the most important ingredients of the fracturing process on a regional length scale (>10 km). The purpose of this article is not to study the seismic sequences resulting with a model of fault interaction; rather, I apply a time-dependent stochastic model with a finite number of states at the length scale of a fault segment in order to capture essential patterns of fault growth such as the geometry of the faults or the deformation accommodated along faults over different time intervals. Then, if the strain rates along the different faults can be quantified, they can be used in the future as the inputs to a model of fault interaction. An important reason for focusing on the development of fault populations is that only through comparison with both tectonic and seismic databases can the prediction of a numerical modelling become more relevant.

Over the last ten years, the modelling of fracture populations has become a well-established approach with a large variety of applications (e.g. reservoir and aquifer characterization, reaction and transport phenomena). It is beyond the scope of this paper to compare in detail the present model with all previous investigations. However, different studies are single out in order to illustrate some advantages of this new model. An & Sammis (1996) have developed a cellular

automaton which reproduces some characteristics of the geometry of crustal shear zones. In this paper, in addition to the shape of a fault population, the local tectonic regime along the faults is analysed. The approach is similar to that of Cowie *et al.* (Cowie *et al.* 1993; Miltenberger *et al.* 1993; Sornette *et al.* 1994; Cowie *et al.* 1995; Cowie 1998) in which the question of the self-organization of an evolving population of fault has been addressed. Nevertheless, in the model presented here, the fault is not defined by a repetition of earthquake ruptures. Instead, the fault zone and the local tectonic regime are defined via a local strain rate determined from the long-term history of the fault system. The idea is that an individual earthquake is an expression of the localization of the deformation but not the cause of such localization. Thus, the microfracturing process integrated over long time periods determines the geometry of the fault and any one earthquake is merely a particular and discontinuous expression of this long-term process. Moreover, this allows the incorporation of the analysis of different modes of dissipation (earthquakes, creep). In fact, aseismic deformation such as post-seismic slip (Langbein 1990), slow earthquakes (Dragert *et al.* 2001) and creep (Simpson *et al.* 2001), may comprise an important part of the deformation that is not included in models that consider only repeated individual earthquakes. Another difference with the approach of Cowie *et al.* (1993) is that all material properties are uniform.

2 A MODEL OF DEVELOPMENT OF A POPULATION OF STRIKE-SLIP FAULTS

The development of the whole system is determined by the orientation of the tectonic loading and the pattern of pre-existing damage. The compressive principal stress orientations are taken to be North-South ((σ_1), vertical (σ_2,) and East–West (σ_3), in such way that only vertical strike-slip fault segments can form. In addition, pre-existing damage favours right-lateral faults and new segments grow following a *main direction*, at an angle Θ from the North (Fig. 1).

2.1 The length scale of a fault segment

A 2-D regular lattice of cells of the length scale $\mathcal{K}$ (hereafter called $\mathcal{K}$-cells) represents a portion of a crustal shear zone. Following Narteau *et al.* (2000), each $\mathcal{K}$-cell is associated with a conceptual picture of a fault zone: a volume within which a myriad of microfractures may develop and organize themselves at all length scales $k, 0 \leq k \leq \mathcal{K}$ (Aviles *et al.* 1987). $\mathcal{L}$ is the size of the regular lattice. The indices $(x, y), x \in [1, \mathcal{L}], y \in [1, \mathcal{L}]$ label the North–South and West–East coordinates, respectively. Every $\mathcal{K}$-cell is noted $C_{(x,y)}^{\mathcal{K}}$. At any time t, $C_{(x,y)}^{\mathcal{K}}$ is defined by its state of fracturing (a boolean variable) and a local strain rate (a scalar $\dot{\varepsilon}(x, y, t)$).

The two possible states of fracturing are (Fig. 1a)

(i) active: the fault segment interacts with adjacent active segments. The fracturing process reaches the length scale $\mathcal{K}$. The local balance between the dissipation and the external forcing sustains a high density of microfractures which are coherently organized at all length scales.

(ii) stable: the fault segment does not interact with adjacent active segments. Two physical representations are invoked. (1) the fracturing process does not reach the length scale $\mathcal{K}$. The local balance between the dissipation and the external forcing sustains a low density of microfractures. They are uniformly distributed throughout the volume and they do not interact coherently. (2) Non-optimal
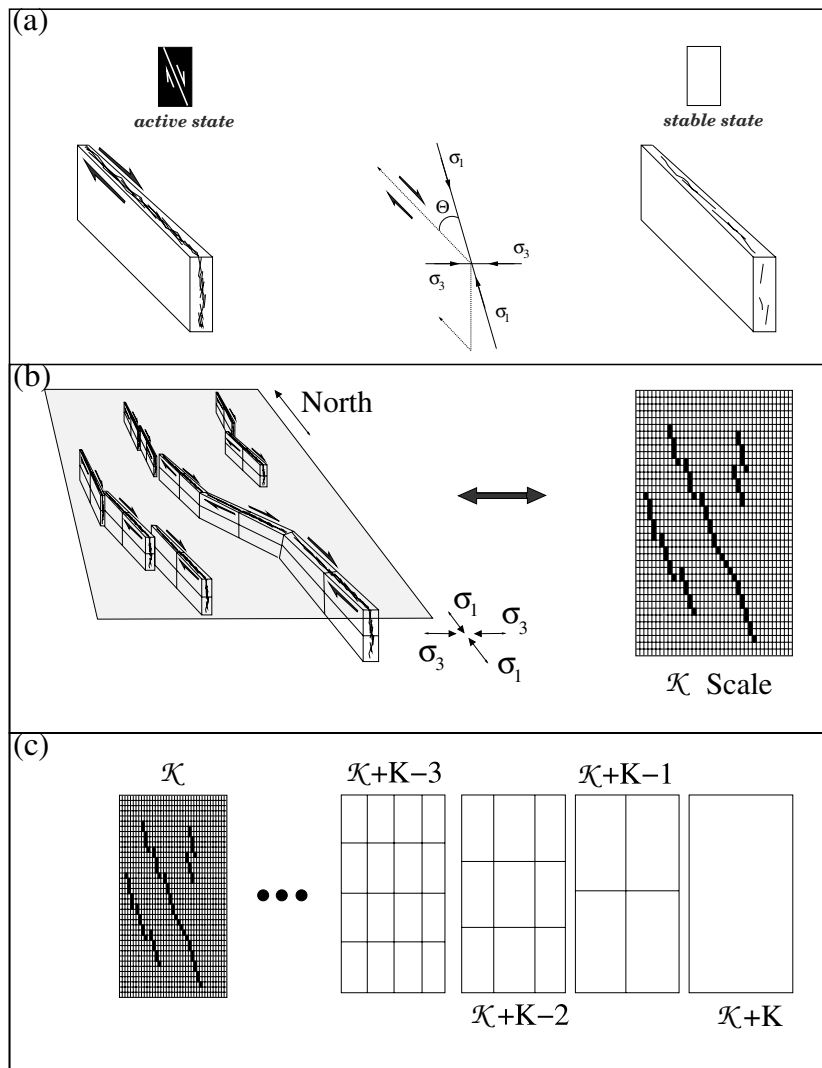
Figure 1. (a) The two states of fracturing used in the model: an active state represents an actively slipping fault segment; a stable state represents an 'intact' zone in which the fracturing process is confined to smaller length scales. σ_1 is north–south, σ_3 is east–west and only vertical dextral strike-slip faulting with an inclination Θ from σ_1 can develop ($\Theta \approx 30^0$). (b) A model of a fault population: within a 2-D regular lattice of stable cells (white cells), the fault network is made of active segments (black cells). σ_1 and σ_3 define the principal axes of the 2-D regular lattice of cells. (c) Schematic representation of the multiscale system: every 2×2 lattice of $\mathcal{K}$-cells, or grid knot, is associated with a $(\mathcal{K} + 1)$-cell. This operation is repeated until a unique cell remains.

geometrical organization at the boundary of the segment temporarily impedes its interaction with adjacent active segments.

The scalar $\dot{\varepsilon}(x, y, t)$ attached to $C_{(x,y)}^{\mathcal{K}}$ is the local strain rate. Ideally, it combines the effect of the external tectonic forcing and fault interactions. $\dot{\varepsilon}_a$ represents the external tectonic forcing and the boundary condition

$$\dot{\varepsilon}_a = \frac{1}{\mathcal{L}^2} \sum_{i=1}^{\mathcal{L}} \sum_{j=1}^{\mathcal{L}} \dot{\varepsilon}(i, j, t) = \text{const.} \tag{1}$$

is maintained throughout the model run to represent the constant external forcing that is observed in geodetic observations of tectonic strain (DeMets *et al.* 1994).

2.2 Evolution of an individual fault segment

At the length scale of a fault segment, the dynamic system is described by a time-dependent stochastic process. This process is de-

fined with respect to non-stationary transition rates between the two states of fracturing.

The transition rate from active to stable is associated with a healing process. In the most general case, the healing rule (change in state from active to stable) would occur at a rate that depends on the local strain rate (positive for strengthening, and negative for weakening). In the present work, for the sake of simplicity, the healing rate is taken as a constant, independent of position and time

$$\alpha_s(x, y) = \gamma. \tag{2}$$

In later work, this simplifying assumption will be relaxed.

$\mathcal{K}$-cells may become active when the local strain rate exceeds a critical value $\dot{\varepsilon}_c$. At the critical strain rate $\dot{\varepsilon}_c$, the density of microfractures within the fault zone is high enough to allow their organization through increasingly larger length scales up to the length scale $\mathcal{K}$ of the fault segment. $\dot{\varepsilon}_c$ at each point in the grid is uniform, and its value does not change with time. The transition rate from stable to

active is:

$$\alpha_c(x, y) = \begin{cases} 0 & \text{for } \dot{\varepsilon}(x, y) \leq \dot{\varepsilon}_c \\ k_a \left(\dfrac{\dot{\varepsilon}(x, y) - \dot{\varepsilon}_c}{\dot{\varepsilon}_c} \right) & \text{for } \dot{\varepsilon}(x, y) > \dot{\varepsilon}_c \end{cases} \quad (3)$$

where k_a is a constant with units of the inverse of a time. α_c depends on the difference between the local strain rate and the threshold of activity. Thus, elements are capable of being active when $\dot{\varepsilon} > \dot{\varepsilon}_c$ and larger strain rates are associated with larger transition rates. Therefore a growing fracture accelerates according to an increasing value of the strain rates at the fracture tip.

2.3 The fault

If a fault segment becomes active, it can be a sub-segment of a fault or a fault nucleus. In either case it interacts with the whole system. The distribution of active cells within the array of stable cells corresponds to a map view of the fault population assuming that every fault zone has a constant width and a depth determined by the thickness of the brittle crust (Fig. 1b). A fault is an isolated set of adjacent segments which can rupture during a single event (Harris & Day 1993). More precisely, faults are defined by the so-called fault-orientation neighbourhood rule (Fig. 2). At the length scale $\mathcal{K}$, two active segments are part of the same fault if they are nearest neighbours or second nearest neighbours in the fault-strike direction.

Fig. 3 shows the most frequent geometric patterns of neighbouring active fault segments in the model and how they are associated with real tectonic structures. Most of the time, parallel fault segments (parallel faulting in Fig. 3) can be produced by the overlapping of faults growing towards each other. On the other hand, fault branching results from a coalescence process occurring at smaller length scales ($k < \mathcal{K}$).

A new fault segment is included in a fault composed of $n_F(\mathcal{K})$ cells (say $C_F^{\mathcal{K}}$). This new fault perturbs the strain rates in its neighbourhood according to its interaction with the other faults.
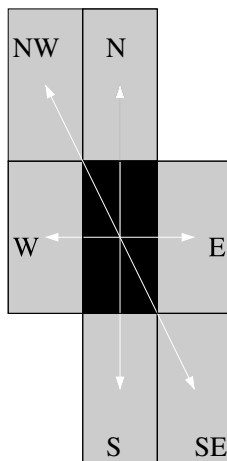

Figure 2. A fault orientation neighbourhood rule in a regular rectangular grid: at the length of a fault segment, active cells aligned in the N–S, E–W and NW–SE directions belong to the same fault of a larger length scale. Six possible connections are noted, N, S, E, W, NW and SE according to the relative positions of the grey-fault segments with respect to the black one (see text and Fig. 3).

2.4 Multiscale system of fault interactions

Geometric rules of fault interaction determine the state of fracturing (active or stable) at larger length scales.

2.4.1 The multiscale system

The multiple scale system is obtained as follow: every 2×2 lattice of $\mathcal{K}$-cells corresponds to a cell of the larger length scale $\mathcal{K} + 1$. The same operation is repeated at increasingly larger length scales until a unique cell of length scale $\mathcal{K} + K$ remains ($K = \mathcal{L} - 1$). Thus, a cell of length scale $\mathcal{K} + n - 1$ is associated with any $n \times n$ lattice of $\mathcal{K}$-cells (Fig. 1c). ($\mathcal{L} - k + \mathcal{K}$) is the size of the regular square lattice of length scale $k \in \{\mathcal{K}, \mathcal{K} + 1, \mathcal{K} + 2, \ldots, \mathcal{K} + K\}$. A cell of length scale k, $C_{(x,y)}^k$, $x \in [1, \mathcal{L} - k + \mathcal{K}]$, $y \in [1, \mathcal{L} - k + \mathcal{K}]$ is a k-cell and $\Lambda_i(C_{(x,y)}^k)$ are the i-cells included in $C_{(x,y)}^k$ ($i < k$) or composed by $C_{(x,y)}^k$ ($i > k$). Thus, $\Lambda_k(C_{(x,y)}^{k+1})$ is the 2×2 lattice of k-cells included in a cell of the larger length scale.

This multiscale system differs from the hierarchical system used in renormalization group theory essentially because the scaling is done at all length scales up to the largest one. Real-space renormalization techniques consist of dividing up a lattice of spacing s into lattices of spacing $\mathcal{R}s$, $\mathcal{R}^2 s$, $\mathcal{R}^3 s$ and so on (Turcotte 1997). Thus the scaling can only be done at an integer power of the renormalization factor $\mathcal{R}$, a positive integer. As a consequence, a cell is included only in one cell at a higher level of hierarchy. In the multiscale system presented in this paper, any cell at a lower scale is included in several neighbouring cells of a higher scale. These intersections of the $\Lambda_i(C_{(x,y)}^k)$ with $i > k$ are key to obtaining any localized patterns within a system with different scales. In particular, this is required to produce the detail of the concentration of the strain rates at all possible growth steps.

2.4.2 The inverse cascade of fault interaction

Lattices with different dimensions represent the brittle crust at different length scales. A k-cell with $k > \mathcal{K}$ can be stable or active, depending on whether or not the internal organization of its fault segments achieves the length scale k. At every appearance or consolidation of an active fault segment at the smallest length scale, the configuration of the $\mathcal{K}$-cells instantaneously determines all the states of fracturing with respect to a rule of interaction applied from the smaller length scale to larger ones (i.e. inverse cascade of fault interaction). Thus a geometric criterion of fault interaction is implemented at all length scales. Based on basic mechanical considerations, this criterion introduces a coarse-graining that may connect two neighbouring faults laterally if they have an overlap to separation ratio greater than one.

In rock mechanics, the full elastic stress field should depend on short-range interactions between neighbouring growing fractures as well as on the long-range interactions imposed by the growth of individual fractures (Rodgers 1980; Mann *et al.* 1983; Mandl 2000). If there is no overlap between two fractures, the simple superposition of the two stress fields is sufficient to describe the interaction. If there is a significant overlap, say l, compared to the crack separation d, the effective length of the crack becomes equivalent to the total length of the two cracks. In the present model, this short range interaction is taken into account and a lateral transfer of the active state is applied at increasingly larger length scales of the multiscale system if $l/d > 1$. This introduces a binary switch that connects the two faults at larger length scales if this condition is met, and neglects the
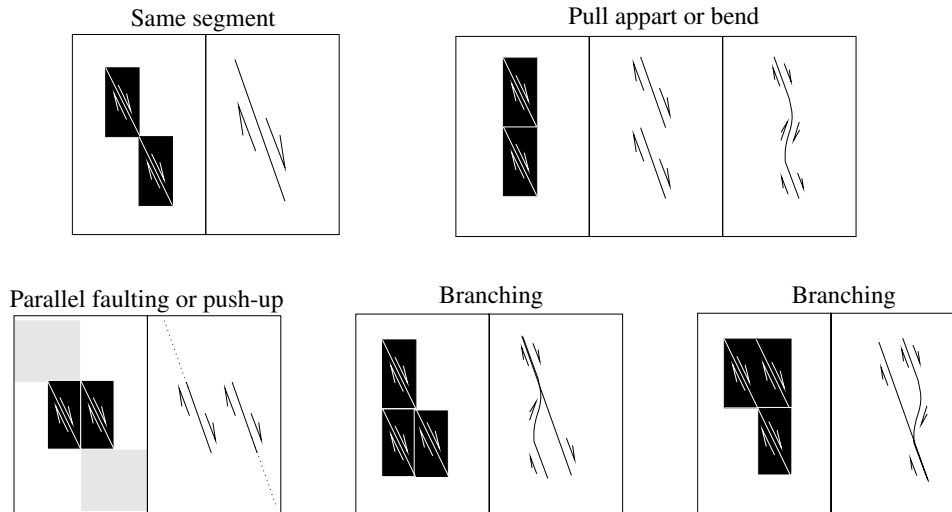
Figure 3. Schematic representations of the faulting patterns associated with different configurations of neighbouring active cells. Parallel faulting is likely to result from external perturbations. For example, it can be associated with the overlapping of parallel growing faults. The two branching examples indicate symmetric fault segment configurations.

interaction if it does not. That is, the magnitude of the redistribution of the strain rates is now proportional to the sum of the strain rates on the two individual segments. The two faults effectively become two segments of a single larger fault at the largest length scale while still retaining their distinctive behaviours at smaller length scales where the overlap to separation ratio is less than one.

In the numerical simulations, a purely geometric failure criterion is applied at increasingly larger length scales. This failure criterion consists of two cooperative configurations of k-cells within $\Lambda_k(C_{(x,y)}^{k+1})$ (Fig. 4a). These configurations involve neighbouring active cells aligned along the N–S or the NW–SE directions. Because active cells model vertical fault segments oriented following the *main direction*, these configurations correspond to the overlap of the shear and extensional zones associated with right-lateral strike-slip motions along each segment. Each cell of these cooperative configurations is oriented 'up' or 'down' with respect to its relative position along the the σ_1-direction (Fig. 4b). This polarity 'up' or 'down' then points in the direction of potential crack growth. $C_{(x,y)}^{k+1}$ is active if one of the upper cells of $\Lambda_k(C_{(x,y)}^{k+1})$ is 'up' or if one of the lower cells of $\Lambda_k(C_{(x,y)}^{k+1})$ is 'down' (Fig. 4c). Thus, at larger length scales, elements are considered active if the upper half of these large element contains at least one 'up' polarity, or the lower half contains at least one 'down' polarity.

Simple examples of the implementation of this inverse cascade of fault interaction are shown in Figs 4(d) and (e). Practically, faults interact positively with one another when, together, they sustain an active cell at a length scale larger than their dimensions. At the length scale of a fault segment, a fault which has a dimension L in the σ_1 direction (i.e. North-South) makes active all the domains located within a rectangular area. This rectangular area is defined by the upper left corner located at $L\,\mathcal{K}$-cells at the left from the northern fault tip and the lower right corner located at $L\,\mathcal{K}$-cells at the right from the southern fault tip (dotted area on Fig. 5). Consequently, if a fault is completely located within the rectangular area of another fault, they do not positively interact together but they can positively interact with other faults. Positive interactions are only possible between two faults which have their tips included in the interacting zones of the other fault. Because of the overlap to sepa-

ration ratio, small fault tips have to be located closer to each other. Thus, within the rectangular area of one fault, the dimension of the interacting zone varies according to the length of the neighbouring faults (dashed area on Fig. 5). Larger zones are associated with longer neighbouring faults and they include all the smaller zones for shorter neighbouring faults.

For any transition from stable to active at the length scale $\mathcal{K}$ of a fault segment, all states are recalculated, and the largest length scale at which a cell experiences a transition from stable to active is defined as k_m.

2.5 Strain rate redistribution

The redistribution rule for the strain rate parameter is based on a simplified template that mimics the basic anisotropy of the redistribution of Coulomb stresses σ_C for a right-lateral strike-slip shear crack. The Coulomb stress is the sum of the mean stress and the product of the local shear stress and the friction coefficient, here taken to be $\mu_c = 0.6$. Theoretically the local stress tensor (from which the normal and shear stresses can be extracted) is related to the distance r from the crack tip, the angle θ from the crack axis, by

$$\sigma_{i,j} = K_k(2\pi r)^{-1/2} f_{i,j}(\theta), \tag{4}$$

where K_k is a stress intensity factor that depends on the mode of fracture. For an isolated crack

$$K_k = Y\sigma l^{1/2}, \tag{5}$$

where Y is a dimensionless geometric constant, σ is the remote applied stress, and l the length scale of the crack. To relate the Coulomb stresses with strain rates, the redistribution is chosen to approximate a viscous rheology. Then, the strain rate variation is equal to the stress variation multiplied by the dynamic viscosity v,

$$\Delta\dot{\varepsilon} = v\Delta\sigma_C. \tag{6}$$

The tectonic rates are redistributed only after the appearance of a new active fault segment in the neighbourhood of the fault along which the stable to active transition has taken place. Along this fault, individual fault segments may line up following the N–S, the
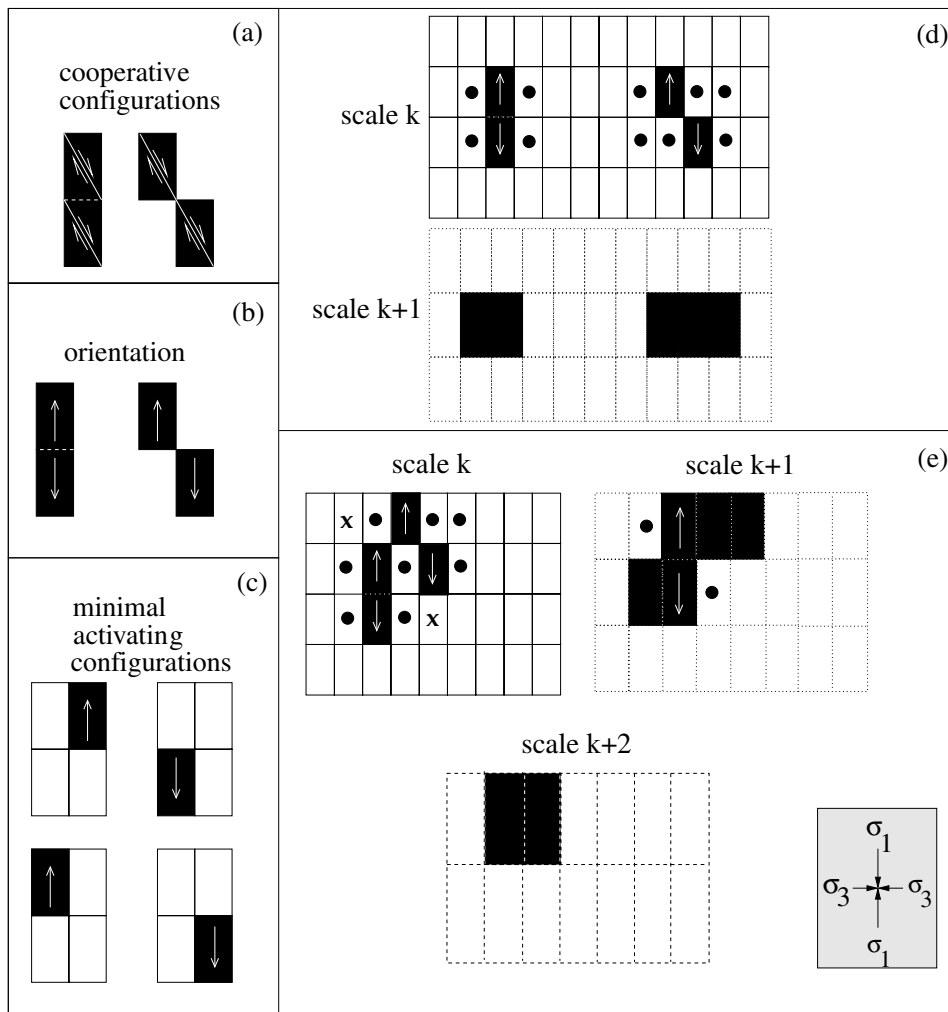
Figure 4. (a) Cooperative configurations of active cells. These configurations are those for which the shear and extensional zones associated with motions along dextral vertical strike-slip fault overlap. (b) Orientation of active cells in cooperative configurations: according to the direction of potential fault growth, the upper cell is 'up' while the lower cell is 'down'. (c) Minimal configurations of active cells that sustain an active state at the larger length scale. (d) and (e) are examples that show how the state of fracturing is determined at increasingly larger length scales. For each example, active cells are in black, stable cells included in an active cell of the larger length scale are marked with a dot, stable cells included in an active cell of the second larger length scale are marked with a cross. Cooperative doublets are oriented. The inset shows the orientations of σ_1 and σ_3.

E–W and NW–SE directions (Fig. 2). Thus three redistribution patterns are associated with these three different geometries of vertical strike-slip faults. These redistribution patterns are a coarse-grained discrete version of the theoretical change in Coulomb stress. Since this fracture problem is rotationally symmetric, four parameters are used to define these redistribution patterns. In a cellular grid, this is the minimum number required to account for an anisotropic redistribution, and the resulting feedback to the strain rate on the active and stable elements. Finally, 12 independent parameters determine the shape of the redistribution (the Q parameters, see Appendix A and Fig. 6). These parameters are fixed so that eq. (6) is maintained and so the inferred stress redistribution is similar to that of a Coulomb redistribution at a macroscopic length scale (see Fig. 6).

To determine the direction of potential fracture growth, each redistribution pattern is divided into two parts. Then, six global masks M^d are associated with each direction $d \in \{N, NW, W, S, SE, E\}$. These masks are applied to all the fault segments composing the fault where the stable to active transition has occured. For an isolated fault segment, these masks are non-zero on the nearest and the next-nearest neighbours. For fault segments of larger faults, these masks are non-zero within larger zones. These zones have a size that varies according to the relative positions of the fault segments along the fault. Their geometries are determined by the shape of the masks according to the local configuration of fault segments (Fig. 6 central column). Thus, the redistribution mechanism can be described as a directe cascade because the geometry of the fault at all length scales determines the local variations of the strain rates and, for example, the spatial extension of the process zone (Fig. 6).

In making calculation, the first step consist of identifying the fault that include the new active fault segment (i.e. C_F^K). After, each fault segment is associated with a matrix which determines the local redistribution process (Fig. 7a). This matrix consists of columns for the NW propagation directions and the SE propagation directions (Fig. 7b). The three components of each column are determined by the geometry of the fault-orientation neighbourhood rule: diagonal (NW and SE),vertical (N and S) or horizontal (E and W). These
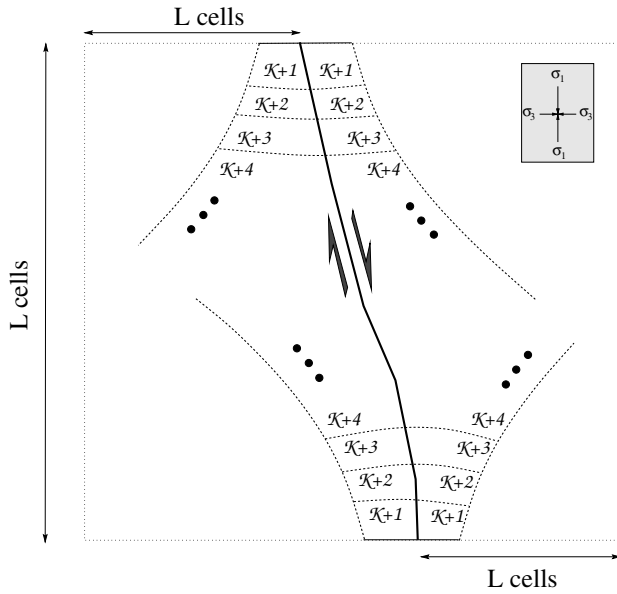
Figure 5. A fault of length L following σ_1 activate all the $\mathcal{K}$-cells located within a rectangular zone. This zone is defined by (1) a top left corner located at L $\mathcal{K}$-cells at the left from the northern fault tip and (2) a bottom right-hand corner located at L $\mathcal{K}$-cells at the right from the southern fault tip (dotted contour). In order to positively interact with this fault, a neighbouring fault has to end within the zones limited by the internal dashed contours. Different contours are for different lengths of neighbouring faults. The number of contours is proportional to L.

element are noted e_i^d, $d \in \{$N, NW, W, S, SE, E$\}$, $i \in C_F^{\mathcal{K}}$. e_i^d is null if the i-cell has no active neighbour in the direction associated with the other column. If e_i^d has an active neighbour in this direction, its value is equal to the size of the square-lattice of $\mathcal{K}$-cells that capture the remainder of the fault in the direction associated with the other column (note the connection with the multiscale system and see examples in Fig. 7c). The NW and SE components are at least 1 to take into account the orientation of a fault segment at the smallest length scale. Each matrix component, $d \in \{$N, NW, W, S, SE, E$\}$, length scale, $m \in [\mathcal{K}, \mathcal{K} + K]$, and $\mathcal{K}$-cell, $a \in [1, \mathcal{L}]$, $b \in [1, \mathcal{L}]$, is associated with a mask $M_{\{m,a,b\}}^d$. Thus, the total strain rate perturbation mask is

$$\Upsilon(x, y) = \rho \dot{\varepsilon}_a \sqrt{k_m} \sum_{o \in C_F^{\mathcal{K}}} \sum_{p \in \{N,...,E\}} M_{\{e_o^p, x_o, y_o\}}^p (x, y) \qquad (7)$$

where ρ is a constant, $\dot{\varepsilon}_a$ is the magnitude of the external forcing system and (x_o, y_o) are the coordinates of the o-cell in the 2-D lattice. Fig. 6 shows Υ for different fault geometries and different values for Q parameters. In Appendix A, note that the strain rate perturbation decays as r^{-2} with respect to the distance from the fault segment (the solution for a point dislocation). The overlapping of the zones of redistribution associated with each segment imposes this decay. When all the masks are applied, near the fault tips, the strain rate perturbation decay as $\sqrt{r}$ (the solution for a crack, eq. 4). Further, the decay of the strain rate perturbation accelerates and far from the fault an exponential decay may be described.

Similar ingredients are present in eqs (4) and (5) and in eq. (7) to account for fracture geometry, fracture length or loading condition. Thus, in the present model, from the transition rates (eqs 2 and 3) and the redistribution of the strain rates (eq. 7) a positive feedback

in the fault growth mechanism may be described. A particularity of the redistribution mechanism developed in this paper is that the geometry of the fault at all length scales controls the shape and the amplitude of the strain rate perturbation. The $\sqrt{k_m}$ dependence in eq. (7) makes the redistribution sensitive to short range interactions between neighbouring faults. In addition, two faults with a similar size may have different strain rates along them. Overall, the activity of a fault depends more on its geometry, its location and its short range interactions than on its length.

The process zone is the neighbourhood of the fault in which the strain rate perturbation is positive. The shadow zone is the neighbourhood of the fault in which the strain rate perturbation is negative. In order to respect the constant external forcing (eq. 1), the redistribution mechanism corresponds to a reorganization of the strain rates that conserves the overall 'tectonic' strain rate $\dot{\varepsilon}_a$. The formation of faults and their growths are then only possible through regions in which strain rates are large enough to create and maintain new active structures. The details of the redistribution of the strain rate are given in Appendix B.

By definition, active fault segments have a high density of microfractures and can be considered weaker than the stable regions between them. Consequently, the strain rates available in the shadow zone are first redistributed along active fault segments and then within the stable region of the process zone. At the end of these transfers, the fault, which is the weakest part of the region where the redistribution takes place, concentrates the remaining strain rates. Thus the evolution of a fault affects the strain rate along neighbouring faults. If a fault is located within the process zone of a growing fault, its strain rates increase. If it is located within the shadow zone, its strain rates decrease. Therefore fault growth is not only possible into a stable region under a significant load but also into the shadow zones of other faults.

In addition to the redistribution process, variations of the strain rates may be due to a diffusion process which allows the system to reach a homogeneous state under extremely low tectonic loading. As in the friction model developed in Narteau *et al.* (2000), the local strain rate heterogeneities slowly decrease in time following a rate asymptotically proportional to the square root of time:

$$\dot{\varepsilon}(x, y, t + \Delta t) = \dot{\varepsilon}_a + \frac{1}{\sqrt{1 + \Gamma \Delta t}} (\dot{\varepsilon}(x, y, t) - \dot{\varepsilon}_a) \qquad (8)$$

where Γ is a reduced diffusion coefficient with units of the inverse of time.

3 EVOLUTION OF FAULT PATTERNS

In the numerical simulations, if an element adjacent to the model boundary becomes active, then the redistribution of the strain rates outside the model grid is neglected. As in conventional laboratory tests, such a zero boundary condition introduces an edge effect where the largest faults grow preferentially in the middle of the model space.

An important aspect of the model is that the time step Δt for each iteration is not constant, but is determined by a generalized Poisson process (see the appendix of Narteau *et al.* (2001)). Thus, for the entire system, the time interval between two events is inversely proportional to the sum of the transition rates,

$$\Delta t = -\frac{1}{\sum_{i=1}^{\mathcal{L}} \sum_{j=1}^{\mathcal{L}} a(i, j)} \log(R). \qquad (9)$$
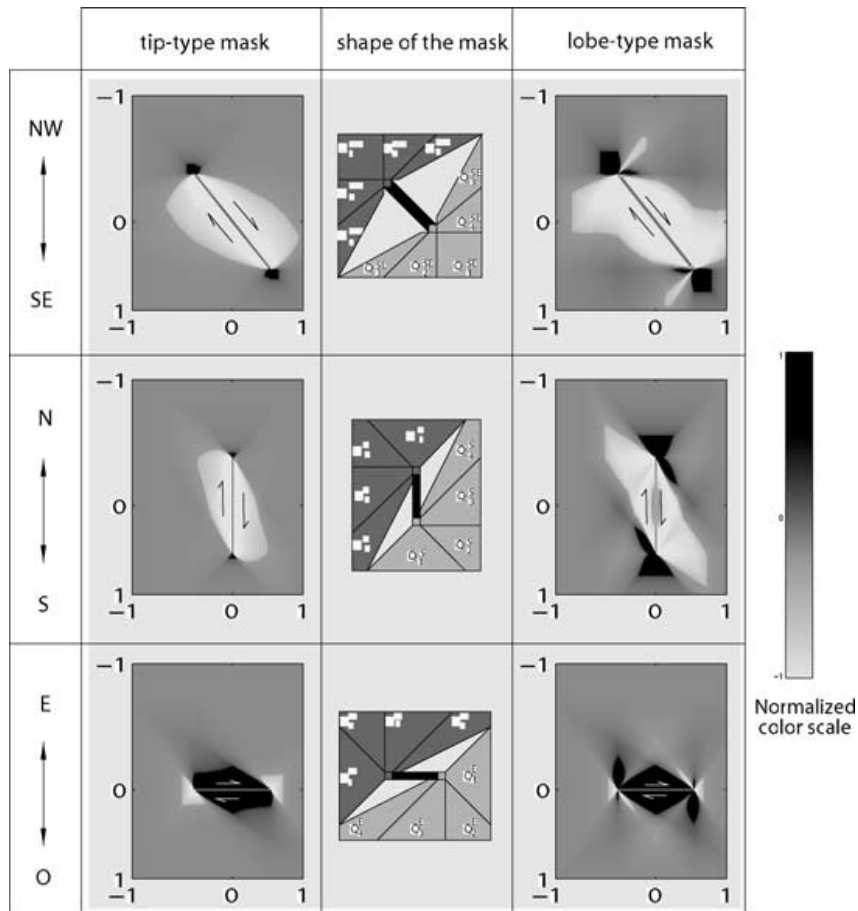
Figure 6. Each line corresponds to an idealized strike of the fault: from top to bottom the fault is successively northwest↔southeast, north↔south, east↔west. The centre column shows a schematic representation of the shape of the masks. The Q parameters are symmetric with respect to the centre of the fault ($Q_i^{NW} = Q_i^{SE}$, $Q_i^{N} = Q_i^{S}$, $Q_i^{W} = Q_i^{E}$). The left and right column show two redistributions for two sets of Q parameters: the tip-type mask ($Q^{NW} = [2, 1, -1, -7]$, $Q^{N} = [1, -4, 0, -1]$, $Q^{W} = [-2, 4, 0, 0]$) generates a process zone at each extremities of the fault and a shadow zone all along the fault; the lobe-type mask ($Q^{NW} = [2, -2.5, 1.5, -7]$, $Q^{N} = [2, -4, -1, 2]$, $Q^{W} = [-0.5, 2, -1.5, 1]$) generates an alternation of process zones and shadow zones with typical lobe-shaped patterns. In this paper, only the the fault tip mask is applied because it results from the simplest coarse-graining technique of the elastic solution.

with

$$a(i, j) = \begin{cases} \lambda_c(i, j) & \text{if the cell is stable,} \\ \lambda_s(i, j) & \text{if the cell is active,} \end{cases} \quad (10)$$

and R a real number randomly chosen between 0 and 1.

At $t = 0$, $\mathcal{K}$-cells are all stable, strain rates are uniform and larger than the critical value $\dot{\varepsilon}_c$ (i.e. $\dot{\varepsilon}_a > \dot{\varepsilon}_c$), so that at least one failure is bound to occur to nucleate the process. Then, the redistribution mechanism produces a heterogeneous strain rate distribution. From eq. (3), the time step depends on the level of concentration of deformation, ensuring that larger fractures grow more quickly, and intact zones at high strain rate break more rapidly.

Once the first element becomes active the chance of a future element making a transition is now not uniform. Instead the next element to make a transition is determined by a weighted probability, where intact elements having a high strain rate are proportionately more likely to become active. For a given time interval this probability is

$$P(x, y) = \frac{a(x, y)}{\sum_{i=1}^{n} \sum_{j=1}^{m} a(i, j)}. \quad (11)$$

Numerically, we define a cumulative step function ranging from 0 to 1, where jumps are proportional to the $P(x, y)$-values. Then, we draw at random a value between 0 and 1. This value falls within a jump of the cumulative step function which determines in turn the cell which experiences a transition.

This temporal procedure amplifies the positive feedback in the loading in a way that mimics the effect of the stress concentration around a growing fracture. The use of a probabilistic discrete technique preserves the condition that only one fault segment is nucleated per time step, while allowing low-probability events to occur occasionally. Each transition is associated with an individual time step. The transition from active to stable does not always occur at the most highly loaded element, and can occasionally occur at the least loaded element (as long as it is above the threshold). Such events may affect the geometry of the fault population over long timescales.
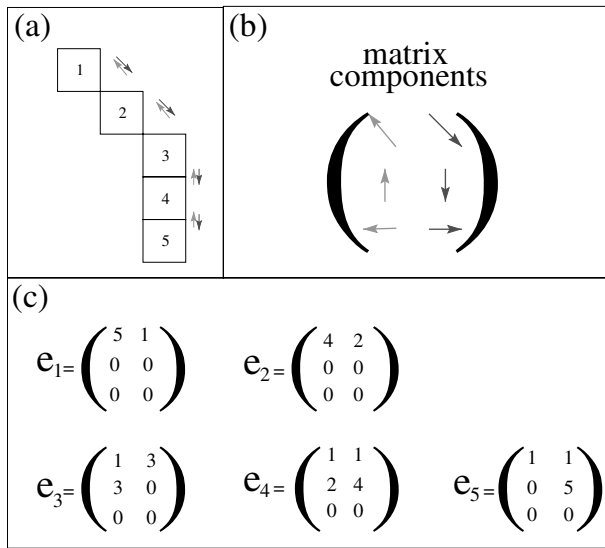
Figure 7. Examples of local stress redistribution matrices for a given fault geometry: (a) the fault geometry composed of 5 $\mathcal{K}$-cells; (b) orientation associated with each component d of the matrix ($d \in \{$N, NW, W, S, SE, E$\}$); (c) for each $\mathcal{K}$-cell i, $i \in [1, 5]$, of the fault, the matrix e_i^d are shown. If the i-cell has an active neighbour in the direction associated with the other column, the e_i^d value is equal to the size of the square-lattice of cells of the elementary scale that capture the remainder of the fault in the direction associated with the other column. If not, e_i^d is null. Because of the strike of a single fault segment e_i^{NW} and e_i^{SE} are at least 1.

After any transition, the cascades are implemented to determine the state of any cell at all length scales, and to determine the amplitude and the shape of the strain rate redistribution in the case of a transition from a stable to an active state.

3.1 Evolution of fault patterns

Fig. 8 shows the evolution of fault patterns under a 'low' tectonic loading: $\dot{\varepsilon}_a/\dot{\varepsilon}_c = 1.01$. All the other parameters of the model are defined in Table 1.

In the description of the numerical simulations, the populations of sub-parallel faults may be called fault networks. Although there is no clear boundary between them, it is possible to distinguish different phases in the evolution of the fault patterns as follows.

3.1.1 The nucleation phase

Isolated active fault segments (e.g. fault nuclei) appear at the initial phase. Since fault interaction is negligible, these fault nuclei have a random homogeneous spatial distribution, and their number increases at a constant rate. The strain rates remain virtually uniform and only small fluctuations can be distinguished in the neighbourhood of the fault nucleus. Nevertheless, they favour the accumulation and the concentration of strain rates on the fault segment and at the fault tips (process zones) while they impede it on each side of the fault (shadow zones). Fault nuclei are indistinguishable from one another, except for their location.

3.1.2 The growth phase

As the nucleation process continues, strain rates are primarily concentrated at the process zones of the fault nucleus. In these process zones, the intensity of the microfracturing process increases and

fractures at all length scales may organize themselves more efficiently. This favours the activation of new fault segments and the growth of the fault. During this growth phase, the fault tips move faster as the fault gets bigger (eq. 3).

Because the amplitudes of the strain rate perturbations induced by the fault nucleus are small, fault interaction cannot generate step-overs during the growth phase. Consequently, new fault segments always interact positively with fault nuclei to form larger faults. During this evolution stage, step-over structures can be produced only randomly by the nucleation process.

The new faults are orientated close to the *main direction* with respect to the shape of the mask. The intensity and the spatial extension of the process zones coupled with the geometry of the fault itself produce a variety of growth patterns along different orientations. Branching may occur if the fault propagates simultaneously in two directions.

Strain rates become more and more heterogeneous. The shadow and process zones cover increasingly larger areas and the variation in the strain rates between these zones increases.

An intrinsic property of the growth process is the production of non-uniform strain rates along the faults. Basically, the strain rates of central segments are larger than the strain rates at the fault tips. This is consistent with geological observation (Cowie & Scholz 1992a). In detail the distribution of the strain rates along faults is more complex. First, the strain rates depend on the local geometry of the fault. The closer the alignment of the fault segments is to the *main direction*, the larger the strain rates are along these segments. Second, the strain rates along faults also depend on the detailed evolution of the fault. The oldest parts of the fault have the largest strain rates, and, due to the growth velocity of each fault tip, the strain rates may have different distributions (see Fig. 9). They are asymmetric with respect to the centre of the fault if one tip propagates faster than the other one (Figs 9a and b). They are symmetric if the tips propagates at the same speed (Fig. 9c). All of these types have been observed in nature (Manighetti *et al.* 2001).

Having started from a completely homogeneous system in the nucleation phase, every fault is unique in the growth phase. In fact, the geometry and the history of the fault both define the characteristics of the strain rate distribution along this fault and its relative activity within the fault network. This differentiation between faults is key for the evolution of the fault population. It may also explain why simplified models based on mean-field solutions assuming identical faults or cracks fail when confronted with actual data, particularly in the later stages of deformation (e.g. the damage model such as Cox & Meredith 1993).

3.1.3 The coalescence and interaction phase

The nucleation process is now almost nonexistent. Isolated fault segments may appear but most of the time they do so within the process zones of large faults. Since their predetermined evolution is to interact with these faults, it is possible to distinguish them from fault nuclei. As the growth process continues, the ratio between the length of the faults and their separation length increases and the faults begin to interact. We can discriminate three types of interaction:

(i) Positive interaction: overlap of process zones when two faults propagate towards the same zone. In this case, the fracturing process is enhanced within this area and results in a coalescence (Fig. 10
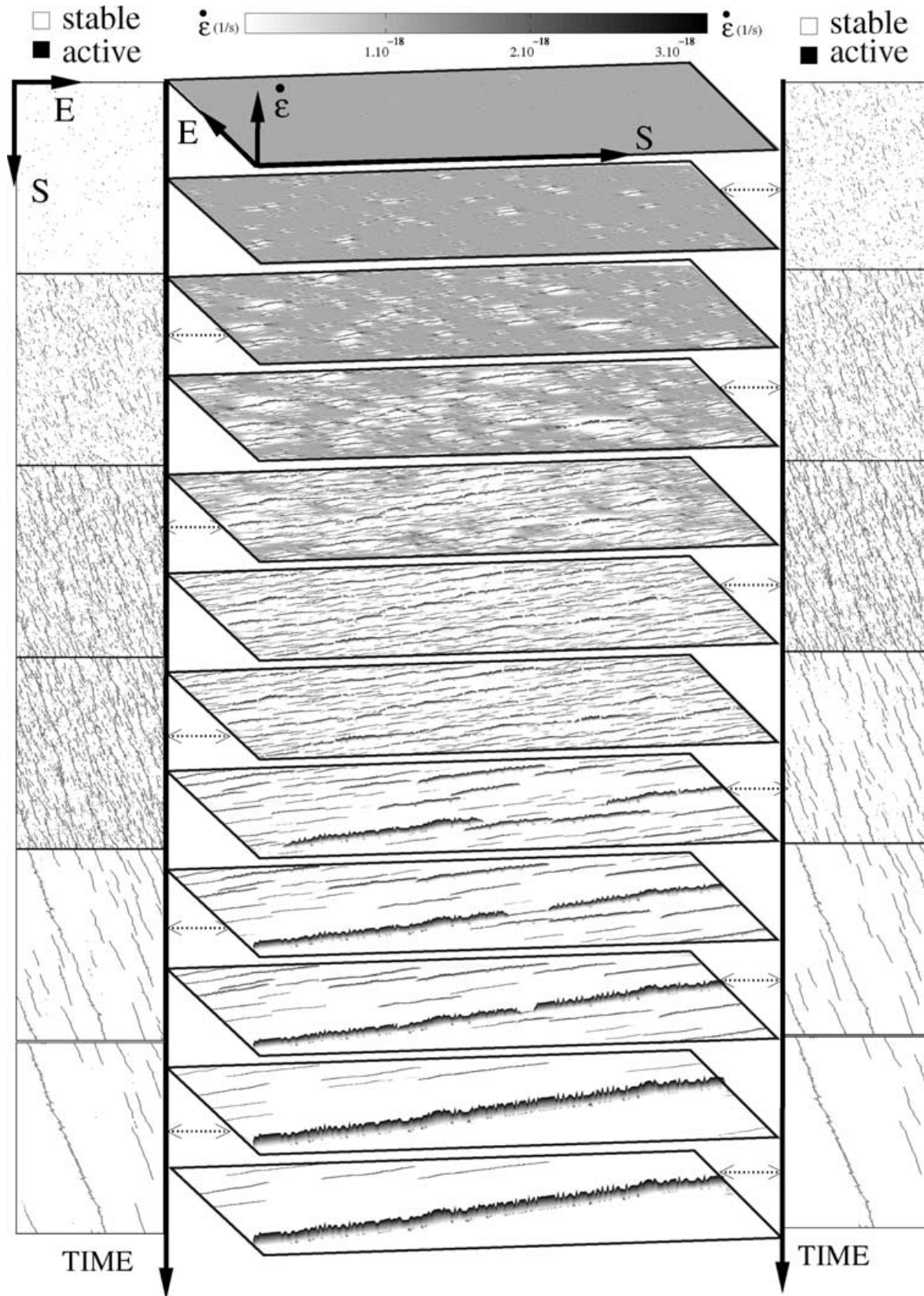
Figure 8. Evolution of fault patterns for $\dot{\varepsilon}_a = 1.01\dot{\varepsilon}_c$ and model parameters defined in Table 1. The central column represents the evolution of strain rates at different times. From the top to the bottom and in Myr, $t = [0.022; 1;4; 7; 12; 17; 23; 30; 40; 51; 57; 62]$. Strain rate variations are larger than allowed by the grey scale and the $\dot{\varepsilon}$ value can reach 5 10^{-16}. At the same times, left and right columns display the state of fracturing of $\mathcal{K}$-cells (see dashed arrows).

Table 1. Model parameter values. Note that, except for the ratio $\dot{\varepsilon}_a/\dot{\varepsilon}_c$, all the parameters remain the same for all numerical simulations.

$\mathcal{L}$	256
$\dot{\varepsilon}_c$	10^{-18} s^{-1}
$\dot{\varepsilon}_a/\dot{\varepsilon}_c$	$\{1.01, \sqrt{10}\}$
k_a	3.15×10^{-13} s^{-1}
γ	3.15×10^{-13} s^{-1}
Γ	10^{-12} s^{-1}
ρ	10^{-1}
Q_i^d	see Fig. 6

zone A) or a competition between process and shadow zones (see point (iii) below and Fig. 10 zone B).

(ii) Negative interaction: overlapping shadow zones when two parallel faults propagate simultaneously. These faults have different growth rates resulting from their respective interactions with other neighbouring faults (see point (i) above). As a consequence, one fault grows faster and dominates the entire region. The dominant major fault takes deformation from other faults which become stable and disappear. Such pattern of interaction gives rise to a slow but certain deactivating of faults.

(iii) Steady interaction: overlap of shadow and process zones when a step-like discontinuity is observed (see Fig. 10 zone B at $t = 15.5$ Myr). The overlap of process zones may result in this steady interaction. These interactions may be stable as long as the faults have similar lengths. In fact, each competes for expansion into the shadow zone of the other. In general, the longest fault will quickly dominate the sub-network and paralyses activity on the other fault (see point (ii) above).

These interactions can efficiently modify the geometry of the fault network and form new faulting patterns. The fault population has now a dense composition of faults over a wide range of spatial scales (Figs 8 and 11). Step-overs appear frequently, faults may coalesce and form bend patterns while other faults may produce en-echelon patterns. By these interactions the propagation of faults is accelerated, decelerated or even arrested. The width
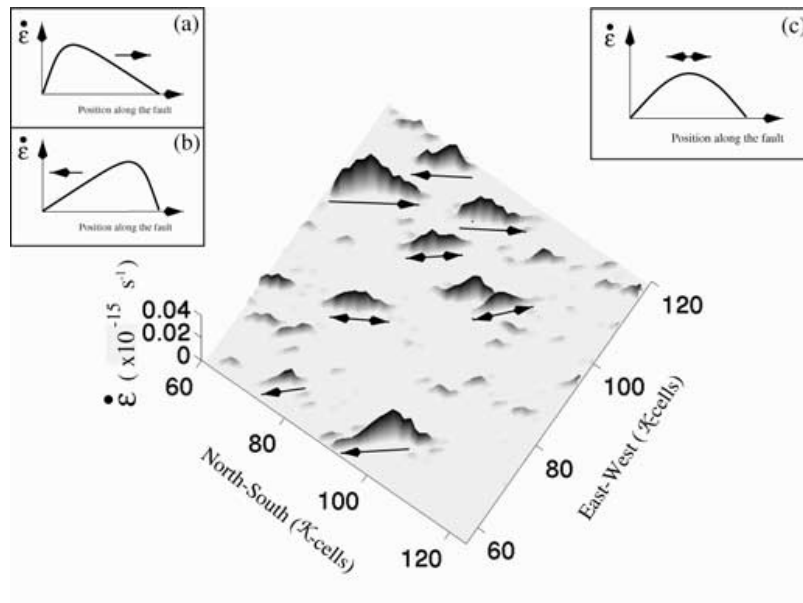

Figure 9. Strain rates at $t = 3.7$ Myr for $\dot{\varepsilon}_a = 1.01\dot{\varepsilon}_c$, $\mathcal{L} = 64$ and model parameters defined in Table 1. For the major structures of this sub-network the arrows point to the younger parts of the faults. The inset (a) and (b) schematically indicate strain rates along faults propagate preferentially in one direction. The inset (c) schematically indicates the strain rates along faults for which each fault tip propagates at the same velocity.
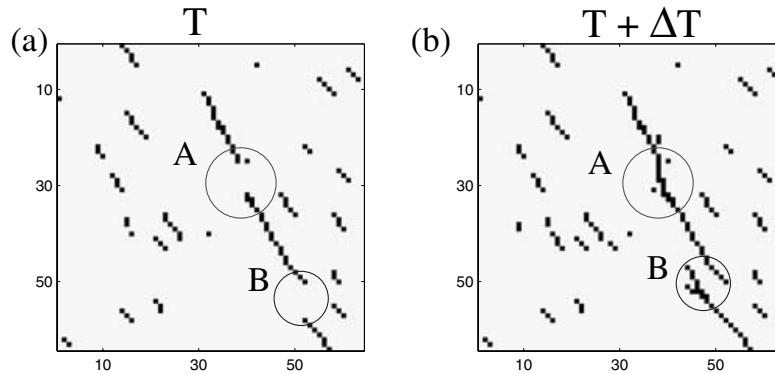

Figure 10. State of fracturing of $\mathcal{K}$-cells at (a) $t = 15$ Myr and (b) $t = 15.5$ Myr for $\dot{\varepsilon}_a = 1.01\dot{\varepsilon}_c$, $\mathcal{L} = 64$ and the model parameters defined in Table 1. In (a), two zones of positive interaction are indicated by circles A and B. In (b), zone A results in a fault coalescence while zone B results in a steady interaction (see point (iii) in text).
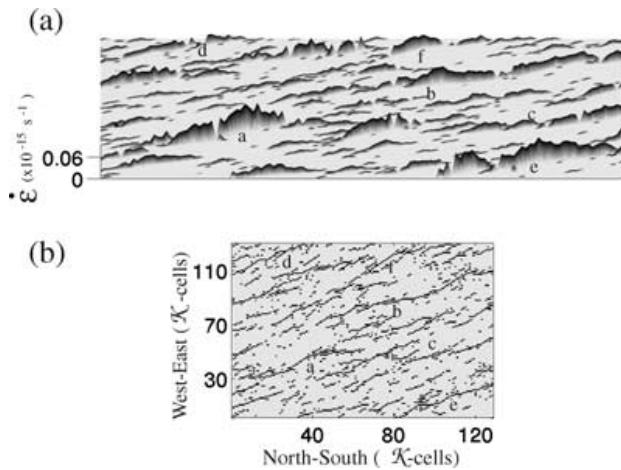
Figure 11. (a) Strain rates and (b) state of fracturing of the $\mathcal{K}$-cells at $t_1 = 19$ Myr for $\dot{\varepsilon}_a = 1.01\dot{\varepsilon}_c$, $\mathcal{L} = 128$ and model parameters defined in Table 1. This subnetwork of faults exhibits different fault patterns representative of the interaction phase. (a) Two fault segments with strong strain rates linked by a connection with low strain rates. (b) Long step-over (pull-apart) where strain rates are partitioned on both faults. (c) En-echelon faults. (d) Bifurcation in one portion of the fault with partitioning of the strain rates. (e) Different segments with different orientations have different strain rates. (f) Large strain rates on an isolated segment with an alignment close to the *main direction*. Note bends and faults with equivalent length and different strain rates.

of the fault length distribution increases and a hierarchy of faults emerges.

During this phase, the strain rates vary strongly in time because interacting faults can now affect the largest length scales of the system. In fact, even if the zone of the strain rate redistribution is proportional to the length of the fault, if it interacts with at least one other, the intensity of the redistribution of the strain rate will increase following the square root of the length scale of the zone they together cover (eq. 7). Consequently, faults with positive or steady interactions evolve most readily and can extend their zone of influence over the entire population of fault.

Finally, the population of faults evolves from a heterogeneous distribution of strain rates to a configuration for which all significant strain rates are confined on active structures (Figs 8 and 11). Major and minor faults can be distinguished. Major faults have high strain rates; minor faults have low strain rates.

Along faults, strain rate heterogeneity increases (Fig. 11). In addition to the bends, the branching and the history of the fault propagation associated with the growth phase, these heterogeneities are due to coalescence and overlap of the shadow and process zones of neighbouring faults. For example, the region which links two faults may be complex in terms of the distribution of strain rates and bifurcations or step-overs may partition the strain rates. However, it is still possible to distinguish the direction of fault propagation from the distribution of strain rates along the faults (see more examples in Fig. 11).

3.1.4 The concentration phase

Nucleation and growth have stopped. From the hierarchy established at the end of the interaction phase, the fault network evolves towards a pseudo stable state based on the coexistence of major faults. During this phase, major faults in steady interaction increase their strain rates by removing the strain rates from minor faults. The duration of this process depends on the geometry of the faults, their respective positions and the strain rates along them. Thus the model predicts the observed 'dead faults' seen in active tectonic zones.

The active fault network becomes less compact (Fig. 8). Major faults of different lengths emerge with increasingly simpler geometry. Branching and step-overs disappear but bends between regular segments may persist. The strain rates remain concentrated on the major faults. During this concentration phase, the longest faults have the largest strain rates. Along these faults, the strain rates become more uniform and may vary according to the alignment of the fault segment with respect to the *main direction* and structural irregularities.

Even if the network has reached a more stable configuration, the fault population continues to evolve. Processes described above (see Sections 3.1.2 and 3.1.3) apply also to the length scale of the major fault. In fact, major faults which are locally in steady interaction may also be in positive interaction with more distant faults. Consequently, zones of positive interaction between two major faults are the places where the propagation and the convergence of these faults occur. Finally, these faults may coalesce to form a megafault with the dimension of the whole system. A megafault absorbs all the strain rates and affects the whole network by shutting other major faults off. The fault population with a megafault and minor faults is extremely resilient despite small fluctuations over long times.

3.1.5 From the nucleation phase to the megafault

During the first stages of development, the population of faults organizes itself to accommodate the tectonic loading. Ultimately, there is a state in which deformation is concentrated on megafaults along which strain rates are uniform. Empirically, this state is most efficient at eliminating excess energy and it can be seen as the best configuration to support tectonic motions. Starting from a homogeneous system, such a fault network cannot be established instantaneously, either in this model, in the laboratory or in the Earth. Rather, the evolutionary process in all these cases includes a nucleation phase, a growth phase, an interaction phase and a concentration phase. The succession of these phases forms a localization process of the deformation resulting from the interrelated evolution of the faults and the distribution of the strain rates (see Section 3.2.1).

3.1.6 Evolution of a megafault: the branching phase

The fault network may also evolve differently under a higher tectonic loading. This evolution of fault patterns is illustrated in Fig. 12. Model parameters are the same as before except for $\dot{\varepsilon}_a/\dot{\varepsilon}_c = \sqrt{10}$.

For a larger amplitude of tectonic loading the nucleation phase activates a larger number of fault nuclei. From this multitude of fault nuclei, the growth phase initially produces a denser fault network. The larger number of faults and the higher amplitude of the tectonic loading results in a more complex distribution of the strain rates and a less regular fault geometry. Fault interactions still favours the concentration of strain rates along a subset of faults. As a hierarchy of fault is established, major faults emerge. They continue to evolve, and, gradually, the localization process regularize their geometry by deactivating minor fault branches. Finally, a megafault is formed because of the propagation towards the north of a major fault. This propagation is facilitated by the positive interaction of the megafault with a minor fault northwest of the network.
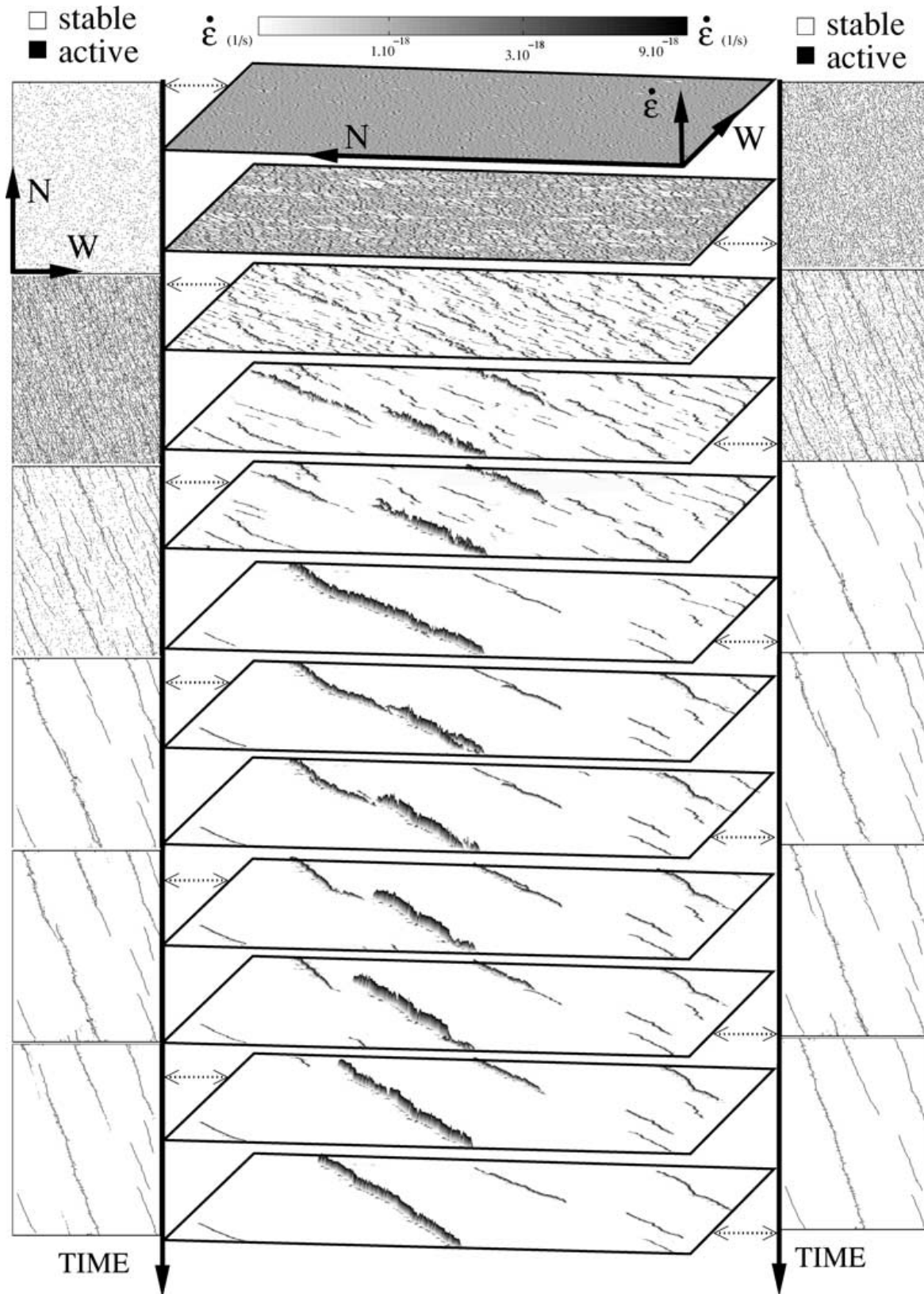
Figure 12. Evolution of fault patterns for $\dot{\varepsilon}_a = \sqrt{10}\dot{\varepsilon}_c$ and model parameters defined in Table 1. The central column represents the evolution of strain rates at different times. From the top to the bottom and in Myr, $t = [2\ 10^{-4}; 10^{-3}; 0.2; 1.5; 2.7; 4.7; 15; 20; 25; 33; 38; 40]$. Actual strain rate variations are larger than allowed by the grey scale and the $\dot{\varepsilon}$ value can reach $1.5\ 10^{-15}$. At the same times, left and right columns represent the state of fracturing of the $\mathcal{K}$-cells (see dashed arrows).

In essence, megafault geometry is irregular because it is an arrangement of segments that have evolved under various configurations. In Fig. 12, it is possible to distinguish three major segments after the megafault has been formed: two parallel southern segments are separated by a bend; a northern segment is present with an alignment closer to the north–south direction than the alignment of the southern segments. These bends and irregularities in the alignment of the fault are associated with low strain rates. This means that, in these areas, the localization process has not been achieved and that the strain is distributed over a larger area. Zones where major segments connect are unstable while the fracturing process is still intense. At the bend between the southern segments, it is possible to distinguish the development of parallel segments from structural disorder. The new fault segments correspond to branches which, if they are stable in time, better satisfy the tectonic loading and the local geometry of the fault network. In Fig. 12, the branching phenomena is first observed along the southern segment. The old branch becomes quickly inactive and concentration of strain is favoured on the new branch. During this process, strain rates partition along each branch of the fault. Later, a new branch also develops towards the north along the central segment but its propagation is slower. In practice, the new branch competes with the previous one. Because the strain rates along these structures are high, neither branch is dominant. The strain rate perturbations associated with their developments are not strong enough. This competition lasts for a long time, and the strain rates along each fault fluctuate. Finally, the new branch dominates the system because of its better alignment and propagates rapidly. The orientation of the new fault is more regular and bends have disappeared. The branching phase erases the irregularity of the fault network with respect to the orientation of the tectonic loading. This may explain why mature faults appear to be smooth along their strike and such a sharp discontinuity perpendicularly to their strike. Since its formation, the evolution of the megafault has consisted of a clockwise rotation of its alignment.

During the evolution of this network, a pull-apart disappears on the major fault located at the north, two faults coalesce at the northeast corner, and two major faults compete with each other at the southeast corner. The youngest fault network presented in Fig. 12 is extremely stable. It does not change for at least the next 100 My, i.e. over a timescale comparable with the lifetime of the present-day plate-tectonic motions (DeMets *et al.* 1994).

3.2 General properties of the evolution of a population of faults

In this section, emergent properties of the model are discussed. These properties result solely from the pattern of interaction between the element of the system over long times because no pre-existing material heterogeneities are determined *a priori*.

3.2.1 The localization process

Over different stages of development of a fault population, Fig. 13 illustrates the localization process by showing the spatial distribution of the transitions from stable to active along a transect line perpendicular to the *main direction* and passing through the centre of the lattice.

From the nucleation to the branching phase, the deformation tends to concentrate on larger and larger faults. These faults extend into their process zones and impede the development of other faults in their neighbourhoods. Because strain rates are higher on pre-
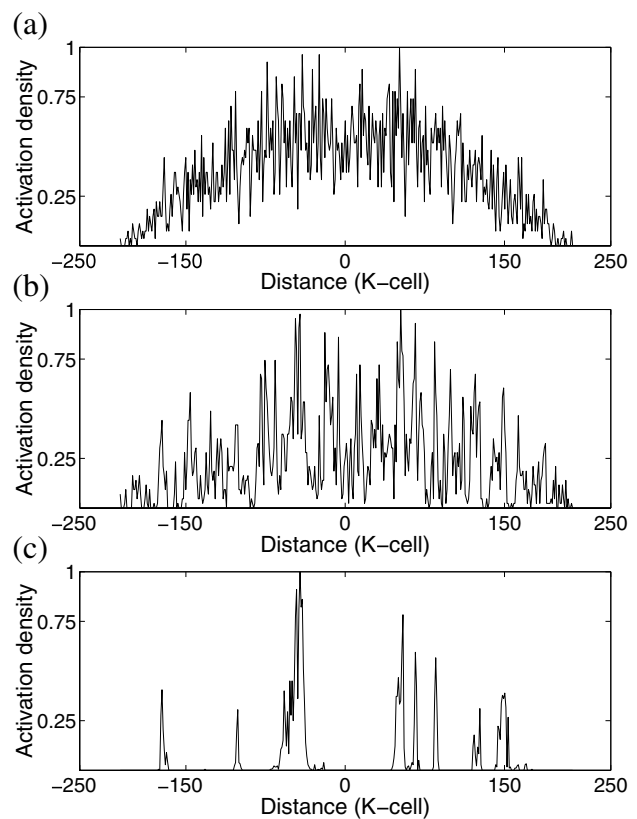

Figure 13. For the simulation presented on Fig. 8, the activation density is plotted over three different time intervals: (a) nucleation phase ($0 < t < 2$ Myr), (b) growth phase ($2 < t < 12$ Myr) and (c) concentration phase ($50 < t < 60$ Myr). The activation density is the normalized distribution of the transitions from stable to active along a transect line perpendicular to the orientation of the megafault and passing by the centre of the lattice.

fractured (or weak) material, the faults accumulate the deformation, extend through increasingly larger areas which, in turn, participate to increase the strain rates along this structure. Consequently, localization is irreversible under constant loading.

The phenomenon of localization of deformation is a ubiquitous property of all the models of granular media and of brittle materials that combine elastic material properties and inelastic behaviour observed in laboratory experiments (i.e. strain-hardening followed strain-softening towards dynamic stress drop). The present model embodies the same physical ideas and the localization results from the interplay between the anisotropy of the redistribution mechanism (elastic) and the local constitutive rule of evolution between two different states of fracturing (plastic).

As shown by Cowie *et al.* (1993), Miltenberger *et al.* (1993) and Sornette *et al.* (1994), the localization may be obtained by a self-organizing process towards a global state corresponding to a global threshold of effective plasticity. Without weakening, this requires strongly heterogeneous material properties which, in their model, predetermine the geometry of the fault population through all the stages of development. Deformation is concentrated on the 'percolation backbone', corresponding to the weakest line of elements in a particular direction. This paper confirms once more the importance of heterogeneity but a distinction is that they are only incorporated at a microscopic scale via statistical fluctuations. Thus, pre-existing material properties do not affect the evolution of the fault
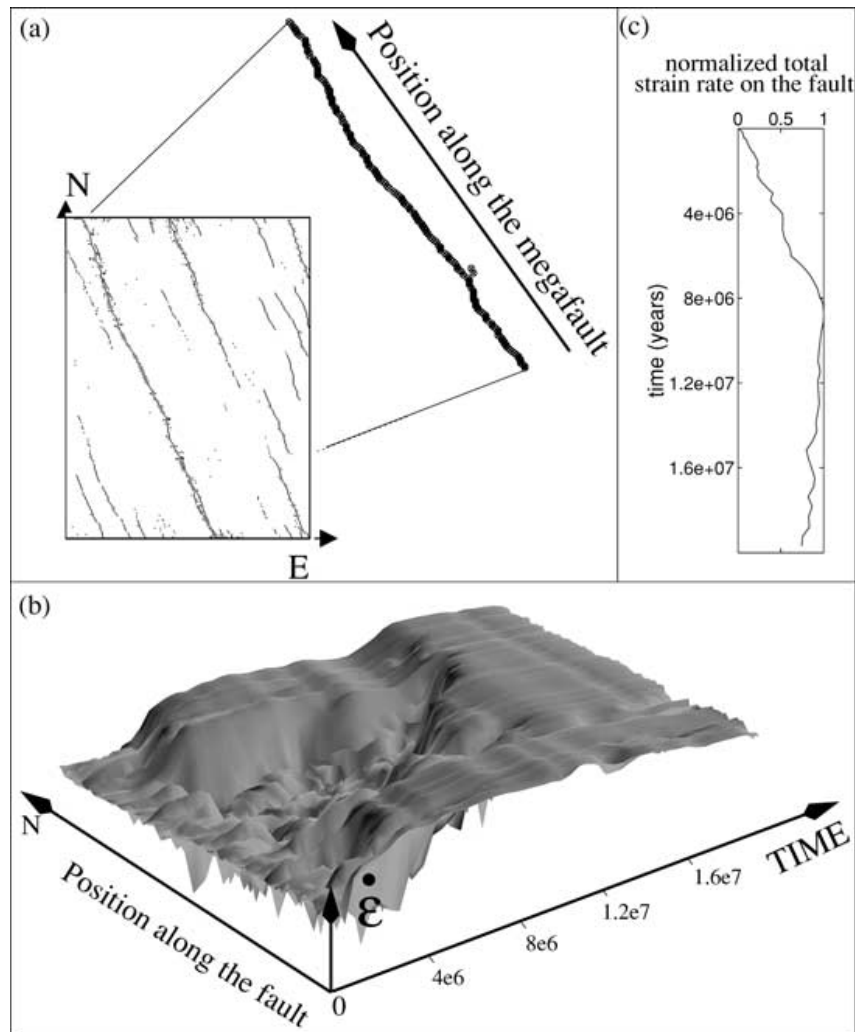
Figure 14. These figures are extracted from the simulation presented in Fig. 12. (a) The megafault trace. It is composed of 186$\mathcal{K}$-cells selected at $t = 18$ Myr from a criteria: a cell is selected if, when it becomes active, (1) it is included in a fault of at least 200$\mathcal{K}$-cells and (2) at least one cell of the length scale $\mathcal{K} + 0.75\mathcal{L}$ becomes active. (b) Evolution of the normalized strain rates along the megafault trace. Homogenization of strain rates follows the formation of the megafault. Note that this homogenization exists also on the southern and the northern segments before the formation of the central segment. The southern segment is more active than the northern one. It is possible to associate the main fluctuation of strain rates with structural irregularities. (c) The total strain rates measured along the megafault trace versus time.

populations in the model presented here. Therefore, the development of the geometry of the fault traces over long times is determined only by the redistribution mechanism. In this way, long-term behaviours are more easily extracted from the output of the model and are shown to be independent of the type of heterogeneity.

3.2.2 Homogenization of strain rates along megafaults

When faults grow, coalesce or interact, the strain rates along them vary. While faults are active, a homogenization of strain rates along these faults is observed. Fig. 14 shows the evolution of the strain rates along the primitive megafault presented in Fig. 12. Immediately following the formation of the fault, the strain rates are uniform along the fault (Fig. 14b) except at major bends. The variation of the total strain rate along the megafault (Fig. 14c) increases monotonously although through a succession of plateaux. At $t = 8.2$ Myr, the total strain rate along the megafault begins to decrease. The plateaux

and the increasing phases are explained by the growth and the coalescence of different fault segments. The decrease indicates the imperfect orientation of the fault with respect to tectonic loading and that the fault is slowly evolving towards a different configuration by branching (see Section 3.1.6).

Under a spatially uniform forcing, the homogenization of the strain rates along the megafaults is regarded as a smoothing process which comes from the relationship between the strain rates and the transition rates (see eqs 2 and 3). In fact, fault segments with larger strain rates are activated more often and redistribute more energy onto neighbouring segments.

3.2.3 Evolution of the deformation along faults

For every $\mathcal{K}$-cell at any time, the cumulative deformation is

$$\mathcal{E}(x, y, t) = \int_0^t \dot{\varepsilon}(x, y, \tau)\, d\tau. \tag{12}$$
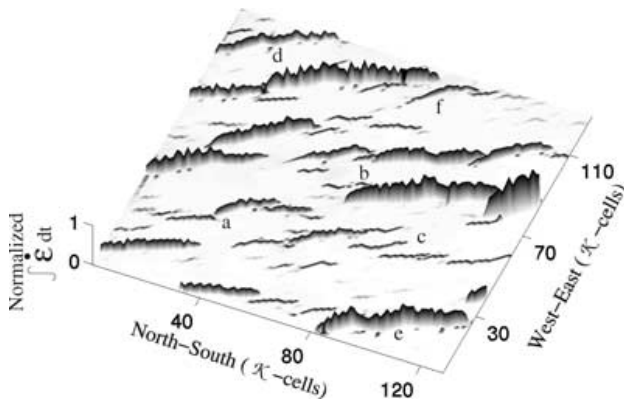
Figure 15. The normalized deformation of the subnetwork presented in Fig. 11. Along faults, strain rates may fluctuate over a wide range of temporal scales. At time $t_1 = 19$ Myr, faults that have the largest strain rates may be not necessarily those that have accommodated most of the deformation. In this figure and in Fig. 11, letters indicate the same structures. (a) Low deformation at a connection between two fault segments; this predominant structure in Fig. 11 is a secondary feature over long times. (b) Long step-over (pull-apart) where the partitioning can be quantitatively estimated; the southern fault is predominant in this system. (c) En-echelon faults: compared to a single fault, this arrangement of fault segments is non-optimum to accommodates the deformation. (d) The bifurcation observed in Fig. 11 is a temporary pattern; the strain rates concentrate essentially on a main trace. (e) Different segments with different orientations can also be identified through the deformation. (f) On a minor fault, the deformation over long times is representative of instantaneous strain rates shown in Fig. 11.

Along any one fault, $\mathcal{E}$ depends on the history of the fault and it quantifies the activity of the fault throughout the development of the fault network.

A quantity integrated over time has properties that differ from any instantaneous picture of this quantity at any point in time. Fig. 15 shows the cumulative deformation $\mathcal{E}$ over the fault population presented in Fig. 11. The comparison between these two figures illustrates the different information contained in each of them. At $t_1 = 19$ Myr, several major faults (with high deformation) are undergoing relatively low strain rates and minor faults are undergoing relatively high strain rates (see caption of Fig. 15 for more details). These phenomena result from switching of activity from one fault population to another. These behaviours are inherent to the dynamic system and indicate the possible complexity of the interrelated evolution of faults within a network. A 'snapshot' $\dot{\varepsilon}$ may or may not be representative of the long-term evolution ε.

Along major faults, the deformation depends on the geometry of the fault, its orientation and history. For the simulation presented in Fig. 8, Fig. 16 shows the evolution of the deformation along the megafault during its formation and evolution. As the megafault forms, two major faults (north and south) are separated by a gap. For each fault the deformation is largest in the central segment and the northern fault accommodates more deformation than the southern fault. These faults propagate slowly towards each other rendering the deformation along them more uniform. Even if there is redistribution of the strain rates within their process zones, the cumulative deformation between the two segments remains extremely low. The coalescence of the northern and the southern faults slowly erases this gap. Different orientations of different fault segments result in variations of the deformation along the fault.

The homogenization of the deformation along a fault is produced by temporary high strain rates along the segment which link the
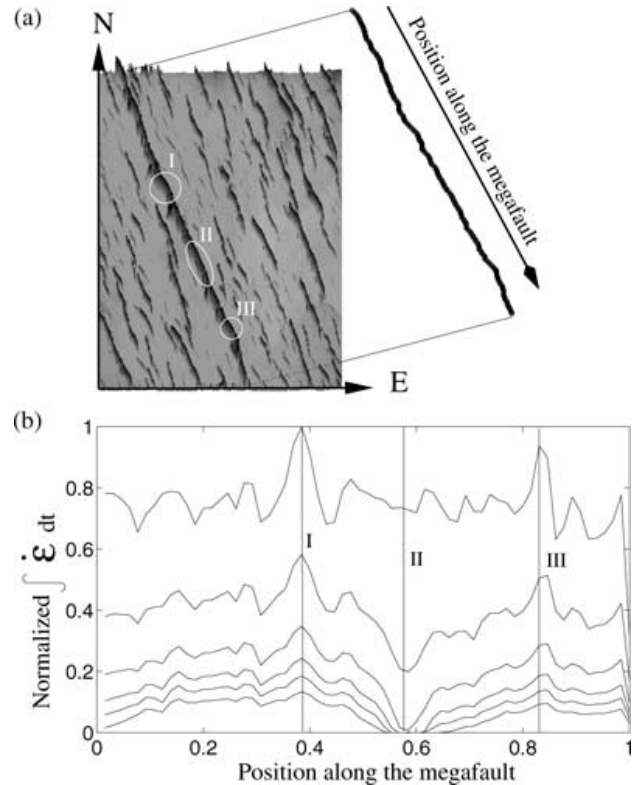

Figure 16. These figures are extracted from the simulation presented in Fig. 8. (a) The megafault trace and the deformation in a logarithmic scale. The megafault is composed of 260$\mathcal{K}$-cells selected at $t = 60$ Myr by the criteria defined in Fig. 14. Zones I, II and III are highlighted. (b) Normalized value of the deformation at $t = [11; 16; 20; 30; 45; 100]$ in Myr. Vertical lines correspond to the centre of zones I, II and III. Comparing with Fig. 8, note that, when the megafault forms, the deformation becomes almost uniform (zone II). Note also that the maxima of the deformation are located along straight segment aligned along the *main direction* (zone I and III).

major faults. A segment connecting two faults is more active during a short time period because it is the only part of the new fault which receives strain rates perturbations from both older fault segments. As shown in Fig. 14, this high activity is only temporary and successive activations of different segments of the fault homogenize the strain rates of the fault (see Section 3.2.2).

3.2.4 Structural regularization

The geometric properties of faults evolve with time (Fig. 17). During the growth phase the fault may propagate in various directions and create branches under different configurations of strain. Later, connection of faults with different orientations, formation of a bend between two parallel faults as well as reactivation of branches due to an external perturbation increase the fault trace complexity. These irregularities of the fault maintain a heterogeneous strain rate distribution but may not satisfy the tectonic loading. Nevertheless, the permanent activity of the fault under such constant external forcing always favours one specific geometry. Over long times, the fault tends to erase its structural complexity. This process may be described as a structural regularization toward the fault configuration which best satisfies the external geometry of the forcing.
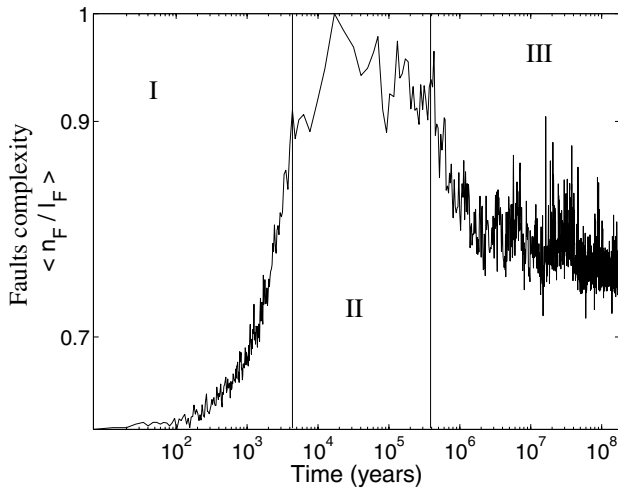
Figure 17. Temporal variation of the complexity of the fault traces. Averaged on 100 consecutive transitions from a stable to an active state, this measure of the fault complexity is the normalized ratio between the number of $\mathcal{K}$-cells included in a fault and the length of this fault. The lower the value of this parameter is, the more regular the fault traces are. This figure is obtained from the simulation presented in Fig. 12. Three periods are indicated. Period I: creation of the faults by nucleation, growth and coalescence. The complexity of the trace increases until it reach a maximum value. Period II: fault interaction and beginning of the concentration of strain rates. The complexity stay almost constant because while some faults continue to develop, the trace of older ones become more regular. Period III: branching phase and megafault evolution. The complexity decreases rapidly to converge towards an asymptotic value.

For the range of parameters presented in this paper, the branching phase may be treated as a subprocess of the structural regularization because it favours a specific orientation of the fault with respect to the tectonic loading.

3.2.5 *Evolution of strain rates per unit of fault length*

The averaged strain rate along the fault is an important property in determining the activity of the fault. For each fault, the evolution of the averaged strain rate may give important indications regarding the future evolution of the network. The relation between the strain rate per unit of fault length versus the length of the fault is presented in Fig. 18. Depending on the length of the fault, three types of variations are observed. Small faults of length $l_F < 0.2\mathcal{L}$ concentrate low strain rates because they do not interact with other faults. These strain rates per unit of fault length increase relatively slowly with length of fault. Faults with lengths ranging from $l_F = 0.2\mathcal{L}$ to $l_F = 0.7\mathcal{L}$ interact with other faults and concentrate higher strain rates. These strain rates per unit of fault length increase more rapidly than during the growth phase. The megafault $l_F > 0.7\mathcal{L}$ does not accumulate higher strain rates per unit of fault length because it results from the coalescence of major faults which have already concentrated all the deformation.

4 DISCUSSION

Starting with a completely homogeneous system, the time-dependent stochastic process outlined in this paper succeeds in reproducing important characteristics of the development of fault systems. Progress in computer power and more precise knowledge
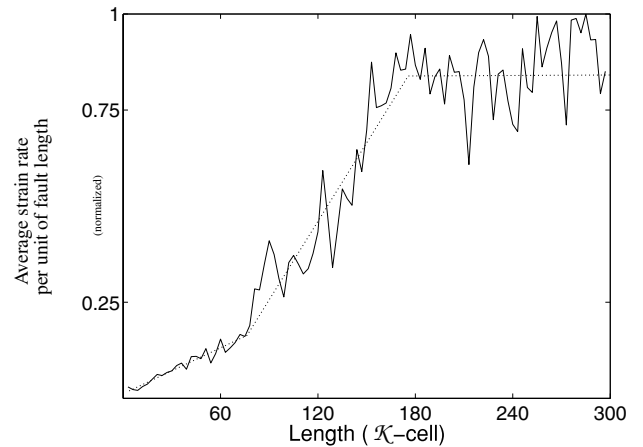
Figure 18. The averaged strain rate per unit of fault length versus the length of the fault. The y-axis is the normalized ratio between the sum of strain rates along the faults and the number of $\mathcal{K}$-cells composing these faults. This figure is obtained from the simulation presented in Fig. 12. For three fault length intervals, dotted segments indicate linear trends corresponding to different phases of development: $l_F \in [0; 70]$, small faults are observed during the nucleation and growth phases; they do not interact with neighbouring faults and concentrate few strain rates. $l_F \in [70; 180]$, major fault formation is observed during the interaction and the concentration phases; they interact with other fault and accommodate more efficiently the deformation. $l_F > 180$, a megafault resulting from the coalescence of major faults is observed; this fault had already concentrated all the strain rates along them and no change of the strain rates density is observed when they coalesce. The plateau corresponds to the amplitude of the external forcing ($\sim \dot{\varepsilon}_a$).

of the crust may perhaps allow incorporation of all types of heterogeneities and the validation of elastodynamic laws under geophysical conditions. Until that time, it is important to provide a general explanation of how a large number of behaviours can be derived from a small number of physical ingredients. In this study, heterogeneities are required to justify the stochastic process. The key point is that these heterogeneities are not predetermined. In fact, the system itself converges towards a stationary statistical state which does not depend on pre-existing material properties. Once this stationary statistical state systematically emerges, characteristic spatial and temporal behaviours related to a whole class of self-organized complex systems can be extracted (e.g. localization, structural regularization, distribution of both strain rates and deformation along faults).

The model shows that when fault growth produces bends, irregularities and different types of unstable configurations between different fault segments, the fault traces may evolve towards another configuration. This evolution implies a partitioning of the strain rates and a competition between parallel branches of the same fault. In the end, the branch with better interactions dominates the other. In this paper, this branching phase has been described at the largest scale of the fault system. In geophysical systems, such internal evolutionary mechanisms may exist. Interestingly, it only requires fault interactions and may occur without rotational conditions or external modifications of the external forcing. In particular, the branching phase offers new perspectives for the modelling of different types of fracture if no quasi-stable configuration can be reached.

Furthermore, the branching phase illustrates an advantage of a time-dependent stochastic approach with uniform material properties. Such a branching mechanism consists of a complete relocation of largest scale faults with either the removal or the formation of

new bends or irregularities along their traces. It may be described as a relocalization of the deformation by reorganization. In a model with heterogeneous failure thresholds, such a behaviour can not be reproduced without an additional strengthening process because the configurations associated with the global threshold of effective plasticity impede a complete relocation of the predominant faults. Then, the final geometry of faults in mechanically heterogeneous model is an optimal interface structure (the percolation 'backbone') which can be determined *a priori* from the spatial distribution of the material properties (Sornette *et al.* 1994). Here, without any pre-determined heterogeneity, the geometries and the orientations of the megafaults are determined by the rules of interaction and the shape of the redistribution. These faults can be located anywhere in response to the statistical fluctuations associated with the time-dependent stochastic process and the limitations imposed by the boundary conditions. Furthermore, the fault traces do not always converge automatically towards an ideal configuration, and can sequentially display different unstable configurations. Such configurations are equiprobable and when the strain rates have transitioned from one fault to another, except by chance, there is no reason for the same fault configuration to become active again.

While the branching phase modifies the largest scale of a fault system, structural regularization is a similar mechanism occurring at smaller scales. Bends, turns and branches of the fault traces may disappear with respect to a smoothing process which, over long times, results from the anisotropy of the redistribution mechanism via the accumulation of the deformation (Wesnousky 1988). Such an observation is difficult to extract from a model with pre-existing material heterogeneities. In fact, the structural regularization can conflict with the optimization process of the fault path. In the present model, because the optimal fault path is a straight line oriented with respect to the tectonic loading, any convergence towards this state can be more easily observed and associated with the structural regularization process.

Material properties which incorporate pre-existing heterogeneities and time-dependent rheologies (weakening or strengthening) are not in contradiction with the stochastic approach. Such additional ingredients can easily be introduced into the modelling if required. For now, it is important to have demonstrated that structural regularization does not require a pre-existing heterogeneity.

A particularity of the model is that the overlap to separation ratio between neighbouring faults is taken into account through the implementation of a geometric interaction criterion at increasingly larger scales of a multiscale system. Thus, in addition to long range interactions, the evolution of the populations of faults also depend on short range interactions between faults situated near to one another. Intuitive rules based on observations and fracture mechanics such as those suggested in this paper have to be tested. They reproduce the same basic behaviours as any other reasonable rules imitating the same phenomena. The purpose is to develop a system in which it is possible to analyse complexity through a limited number of parameters. This practical approach complements traditional ones and offers the possibility of discussing the evolution of geophysical systems over a wide range of temporal and spatial scales.

This paper focuses on the properties of fault populations as well as on the properties of any fault within these fault populations. At any time, it is possible to describe how the strain rates are distributed over different faults. These tectonic rates, integrated over different time intervals, determine the deformation along the faults on different timescales. Instantaneous and integrated pictures of the

system could be compared to geodetic and geological observations within active tectonic regions. If such variations in strain rates exist along real faults, it is important to consider them for time dependant assessment of earthquake hazards. The model presented here can propose and classify these interpretations from the structural patterns observed in a population of strike-slip faults. Simultaneously, its predictions could be used to look for new observations in natural exposures.

In the present model, it is possible to analyse the competition between faults via the partition of the strain rates but not via the temporal distribution of earthquakes (Lee *et al.* 1999). In fact, only the distribution of strain rates over a population of interacting faults has been taken into account. Future work will concentrate on seismic patterns at different stages of the evolution of a population of faults. The idea is to develop a general model that couples a previous model of seismicity presented in Narteau (2006) and the model of development of a fault population presented in this paper. Interestingly, they complement each other and could together provide a global description of the spatial-temporal properties of stress dissipation within a crustal shear zone. In a general seismotectonic model, instead of considering a homogeneous loading and heterogeneous failure threshold, the present model will allow the introduction of heterogeneous loading rates which result from fault interactions at all stages of the development of a population of faults.

In Narteau (2006), at the length scale $\mathcal{K}$ of a fault segment, it is possible to relate different seismic behaviours of a fault zone with the magnitude of a non-dimensional parameter A. This parameter is the ratio between the loading rate and the product of the healing rate and the local stress drop. If $A \approx 1$, the system is in a critical state and large events can occur over a wide range of temporal scales; if $A < 1$, the system is in a subcritical state controlled by faulting and seismic precursors are frequently observed; if $A > 1$, the system is in a subcritical state controlled by healing and the fault zone may be creeping. One particular feature is that the magnitude of the stress stored in the fault zone decreases and the proportion of large events increases as the critical point is approached. This has been interpreted as a weakening process.

If the healing rate and the local stress drop are assumed to have a constant and uniform value, the strain rate used in the present model will be proportional to the parameter A used in Narteau (2006). In this case, from the results of both models, it is possible to infer a general scenario and to conclude the following.

The increase in fault dimension enables the propagation of larger earthquakes. Consequently, over the development of fault populations such as presented in this paper, increasingly larger events can be expected. Moreover, because fault segments under a critical regime (i.e. $A \approx 1$) have a greater proportion of large ruptures, neighbouring fault segments may become critical as following.

(i) Along segments with $A > 1$, it is because large and discontinuous stress dissipations may temporally favour the strengthening, and, so, produce a delayed but significant seismic activity.

(ii) Along segments with $A < 1$, it is because the slip may be directly triggered by stress perturbations associated with the rupture front propagation along an adjacent segments.

Finally, if some parts of the fault are in a critical state, the seismic regime of the entire fault network may become critical. Then, the weakening process observed at the length scale of a fault segment is likely to occur at larger length scales. Such, a weakening process accelerates localization of the deformation along pre-existing faults which tends to grow (see the beginning of the paragraph).
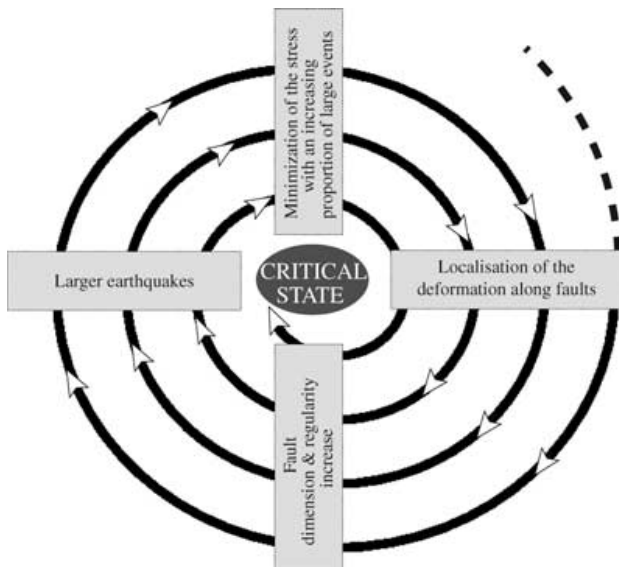
Figure 19. Schematic diagram of the different processes and phenomena that may be sequentially involved in a convergence towards a critical state.

From these inferences, it is possible to conclude that a fault system could be spontaneously attracted to a critical point (Fig. 19). Towards this critical point, the maximum fault dimension increases, the relative frequency of large events is higher, and the break of slope of the frequency–magnitude relationship of earthquakes occurs at progressively larger magnitudes. Seismic activity along the zones of mechanical failure increases the heterogeneities of the stress and larger faults may be able to slip at lower stresses. Thus, the stress is statistically lower in the fault zones and globally lower in the crust. This convergence towards the critical point seems to follow a general principle of minimization of energy.

5 CONCLUSION

A multiscale model of rupture of a crustal shear zone under constant external forcing reproduces various structural properties observed in the formation and evolution of a population of strike-slip faults. At the smallest length scale, the development of this dynamic system is determined by a time-dependent stochastic process with two states of fracturing (active and stable). At larger length scales, the state of fracturing is determined by purely geometric rules of fault interaction based on fracture mechanics. In addition to these short range interactions, a redistribution mechanism in the neighbourhood of active faults ensures long range interactions. Thus, non-linear feedback processes are incorporated in the fault growth mechanism.

Numerical simulations are performed with uniform material properties. This approach demonstrates that pre-determined heterogeneities are not required to produce characteristic faulting patterns and the various phases of development of a fault population. Nucleation, growth, branching, interaction and coalescence are seen as successive expressions of a more general process of localization. A structural regularization process results from the anisotropy of the redistribution mechanism via the accumulation of the deformation. The model predicts that a complete relocation of major fault is possible without invoking rotational conditions or modification of the external forcing. This is described as a branching process involving partitioning of the strain rates and competition between faults. Possible relationships between the seismic regime and the geometry of

the fault population suggest that the fault system may be attracted by a critical point. Towards this critical point, fault dimension increases, the relative frequency of large events is higher and larger faults are able to slip at lower stresses.

REFERENCES

Allègre, C.J., Le Mouël, J.L. & Provost, A., 1982. Scaling rules in rock fracture and possible implications for earthquake prediction, *Nature,* **297,** 47–49.

An, L.-J., & Sammis, C.G., 1996. A cellular automaton for the development of crustal shear zones, *Tectonophysics,* **253,** 247–270.

Aviles, C.A., Scholz, H. & Boatwright, J., 1987. Fractal analysis applied to characteristic segments of the San Andreas Fault, *J. geophys. Res.,* **92,** 331–344.

Clark, R. & Cox, S., 1996. A modern regression approach to determining fault displacement-length scaling relationships, *Journal of Structural Geology,* **18,** 147–152.

Cowie, P., 1998. A healing-reloading feedback control on the growth rate of seismogenic faults, *Journal of Structural Geology,* **20,** 1075–1087.

Cowie, P. & Scholz, C., 1992a. Displacement-length scaling relationship for faults: data synthesis and discussion, *Journal of Structural Geology,* **14,** 1149–1156.

Cowie, P. & Scholz, C., 1992b. Growth of faults by accumulation of seismic slip, *J. geophys. Res.,* **97,** 11 085–11 096.

Cowie, P., Vanneste, C. & Sornette, D., 1993. Statistical physics model for the spatio-temporal evolution of faults, *J. geophys. Res.,* **98,** 21 809–21 821.

Cowie, P., Sornette, D. & Vanneste, C., 1995. Multifractal scaling properties of a growing fault population, *Geophys. J. Int.,* **122,** 457–469.

Cox, S. & Meredith, P., 1993. Microcrack formation and material softening in rock measured by monitoring acoustic emissions, *Int. J. Rock Mech. Min. Sci. &Geomech. Abstr.,* **30,** 11–24.

DeMets, C., Gordon, R.G. & Vogt, P., 1994. Location of the Africa-Australia-India triple junction and motion between the Australian and Indian plates; results from an aeromagnetic investigation of the central Indian and Carlsberg ridges, *Geophys. J. Int.,* **119,** 893–930.

Dragert, H., Wang, K. & James, T., 2001. A silent slip event on deeper Cascadia subduction interface, *Science,* **292,** 1525–1528.

Gupta, A. & Scholz, C., 2000. A model of normal fault interaction based on observations and theory, *Journal of Structural Geology,* **22,** 865–879.

Harris, R.A. & Day, S., 1993. Dynamics of fault interactions: parallel strike-slip faults, *J. geophys. Res.,* **98,** 4461–4472.

Kadanoff, L., 1966. The introduction of the idea that exponents could be derived from real-space scaling arguments, *Physics,* **2,** 263.

Langbein, J.O., 1990. Post-seismic slip on the San Andreas Fault at the northwestern end of the 1989 Loma Prieta earthquake rupture zone, *Geophys. Res. Lett.,* **17,** 1223–1226.

Lee, M.W., Sornette, D. & Knopoff, L., 1999. Persistence and quiescence of seismicity on fault systems, *Phys. Rev. Lett.,* **20,** 4219–4222.

Mandl, G., 2000. *Faulting in brittle rocks,* Springer.

Manighetti, I., King, G., Gaudemer, Y., Scholz, C. & Doubre, C., 2001. Slip accumulation and lateral propagation of active normal fault in Afar, *J. geophys. Res.,* **106,** 13 667–13 696.

Mann, P., Hempton, M. & Dwight, C., 1983. Development of pull-apart basins, *J. Geol.,* **91,** 529–554.

Miltenberger, P., Sornette, D. & Vanneste, C., 1993. Fault self-organization as optimal random paths selected by critical spatio-temporal dynamics of earthquakes, *Phys. Rev. Lett.,* **71,** 3604–3607.

Narteau, C., 2006. Classification of seismic patterns in a hierarchical model of rupture: a new phase diagram for seismicity, *Geophys. J. Int.,* doi:10.1111/j.1365-246X.2006.03212.x.

Narteau, C., Shebalin, P., Holschneider, M., Le Mouël, J.L. & Allègre, C.J., 2000. Direct simulation of the stress redistribution in the scaling organization of fracture tectonics, *Geophys. J. Int.,* **141,** 115–135.

Narteau, C., Le Mouël, J.-L., Poirier, J., Sepúlveda, E. & Shnirman, M.G., 2001. On a small scale roughness of the core-mantle boundary, *Phys. Earth planet. Int.,* **191,** 49–61.

Peacock, D. & Sanderson, D.J., 1991. Displacement, segment linkage and relay ramps in normal fault zones, *Journal of Structural Geology,* **13,** 721–731.

Reynolds, P., Klein, W. & Stanley, H., 1977. Renormalization group for site and bond percolation, *Phys. C,* **10,** 167–172.

Rockwell, T., Lindvall, S., Herzberg, M., Murbach, D., Dawson, T. & Berger, G., 2000. Paleoseismology of the Johnson Valley, Kickapoo, and Homestead Valley faults, *Bull. seism. Soc. Am.,* **90,** 1200–1236.

Rodgers, D., 1980. Analysis of pull-apart basin development produced by en-enchelon strike-slip faults, *Special publication of the I.A. of Sedimentologists,* **4,** 27–41.

Schlische, R., Young, S., Ackerman, R. & Gupta, A., 1996. Geometry and scaling relations of a population of very small rift related normal faults, *Geology,* **24,** 683–686.

Simpson, R.W., Lienkaemper, J.J. & Galehouse, J.S., 2001. Variations in creep rate along the Hayward Fault, California, interpreted as changes in depth of creep, *Geophys. Res. Lett.,* **28,** 2269–2272.

Sornette, D., Miltenberger, P. & Vanneste, C., 1994. Statistical physics of fault patterns self-organized by repeated earthquakes, *Pure appl. Geophys.,* **142,** 491–527.

Turcotte, D.L., 1997. *Fractals and Chaos in Geology and Geophysics,* Cambridge University Press, Cambridge.

Van der Woerd, J. *et al.*, 2000. Uniform slip-rate along the Kunlun Fault: implications for seismic behaviour and large-scale tectonics, *Geophys. Res. Lett.,* **27,** 2353–2356.

Wesnousky, S., 1988. Seismological and structural evolution of strike-slip faults, *Nature,* **335,** 340–343.

APPENDIX A: THE MASKS

The six masks used in the redistribution of the strain rates are

$$
\begin{aligned}
M^N_{\{m,a,b\}}(x,y) = \sum_{i=1}^{m} \frac{1}{i^2} \big(& Q^N_1 \xi^{a+i-1}_{a-i+1}(x)\xi^{b-i}_{b-i}(y) + \xi^{a-i}_{a-i}(x)\big(Q^N_2 \xi^{b-1}_{b-i}(y) \\
& + Q^N_3 \xi^{b+i-1}_b(y) + Q^N_4 \xi^{b+2i-1}_{b+i}(y)\big)\big),
\end{aligned}
\tag{A1}
$$

$$
\begin{aligned}
M^{NW}_{\{m,a,b\}}(x,y) = \sum_{i=1}^{m} \frac{1}{i^2} \big(& \xi^{b-i}_{b-i}(y)\big(Q^{NW}_1 \xi^{a-1}_{a-i+1}(x) + Q^{NW}_2 \xi^{a+i-1}_a(x) + Q^{NW}_3 \xi^{a+2i-1}_{a+i}(x)\big) \\
& + \xi^{a-i}_{a-i}(x)\big(Q^{NW}_1 \xi^{b-1}_{b-i}(y) + Q^{NW}_4 \xi^{b+i-1}_b(y) + Q^{NW}_3 \xi^{b+2i-1}_{b+i}(y)\big)\big),
\end{aligned}
\tag{A2}
$$

$$
\begin{aligned}
M^{W}_{\{m,a,b\}}(x,y) = \sum_{i=1}^{m} \frac{1}{i^2} \big(& Q^{W}_1 \xi^{a-i}_{a-i}(x)\xi^{b+i-1}_{b-i+1}(y) \\
& + \xi^{b-i}_{b-i}(y)\big(Q^{W}_2 \xi^{a-1}_{a-i}(x) + Q^{W}_3 \xi^{a+i-1}_a(x) + Q^{W}_4 \xi^{a+2i-1}_{a+i}(x)\big)\big),
\end{aligned}
\tag{A3}
$$

$$
\begin{aligned}
M^{S}_{\{m,a,b\}}(x,y) = \sum_{i=1}^{m} \frac{1}{i^2} \big(& Q^{S}_1 \xi^{a+i-1}_{a-i+1}(x)\xi^{b+i}_{b+i}(y) + \xi^{a+i}_{a+i}(x)\big(Q^{S}_2 \xi^{b-i}_{b-2i+1}(y) \\
& + Q^{S}_3 \xi^{b}_{b-i+1}(y) + Q^{S}_4 \xi^{b+i}_{b+1}(y)\big)\big),
\end{aligned}
\tag{A4}
$$

$$
\begin{aligned}
M^{SE}_{\{m,a,b\}}(x,y) = \sum_{i=1}^{m} \frac{1}{i^2} \big(& \xi^{b+i}_{b+i}(y)\big(Q^{SE}_1 \xi^{a+i-1}_{a+1}(x) + Q^{SE}_2 \xi^{a}_{a-i+1}(x) + Q^{SE}_3 \xi^{a-i}_{a-2i+2}(x)\big) \\
& + \xi^{a+i}_{a+i}(x)\big(Q^{SE}_3 \xi^{b-i}_{b-2i+2}(y) + Q^{SE}_4 \xi^{b}_{b-i+1}(y) + Q^{SE}_1 \xi^{b+i}_{b+1}(y)\big)\big),
\end{aligned}
\tag{A5}
$$

$$
\begin{aligned}
M^{E}_{\{m,a,b\}}(x,y) = \sum_{i=1}^{m} \frac{1}{i^2} \big(& Q^{E}_1 \xi^{a+i}_{a+i}(x)\xi^{b+i-1}_{b-i+1}(y) \\
& + \xi^{b+i}_{b+i}(y)\big(Q^{E}_2 \xi^{a+i}_{a+1}(x) + Q^{E}_3 \xi^{a}_{a-i+1}(x) + Q^{E}_4 \xi^{a-i}_{a-2i+1}(x)\big)\big),
\end{aligned}
\tag{A6}
$$

with

$$
\xi^{v}_{u}(w) = \begin{cases} 1 & \text{if } w \in [u,v] \text{ with } 0 < u \leq v, \\ 0 & \text{otherwise,} \end{cases}
$$

and Q^d_i, $d \in \{N, NW, W, S, SE, E\}$, $i \in \{1, 2, 3, 4\}$, parameters defined in Fig. 6.

APPENDIX B: STRAIN RATE REDISTRIBUTION

The total strain rates perturbation mask is

$$\Upsilon(x, y) = \rho \dot{\varepsilon}_a \sqrt{k_m} \sum_{o \in C_F^{\mathcal{K}}} \sum_{p \in \{N, \dots, E\}} M_{\{e_o^p, x_o, y_o\}}^p (x, y) \tag{B1}$$

with ρ a constant, $\dot{\varepsilon}_a$ the amplitude of the external forcing, $C_F^{\mathcal{K}}$ the elementary cells composing the fault F, and (x_o, y_o) the coordinates of the o-cell in the 2-D lattice.

The total stress rate perturbation mask may be decomposed into a process zone mask and a shadow zone mask:

$$\Upsilon(x, y) = \underbrace{\Upsilon_{\mathcal{P}}(x, y)}_{\text{process zones}} + \underbrace{\Upsilon_{\mathcal{S}}(x, y)}_{\text{shadow zones}} \tag{B2}$$

with,

$$\Upsilon_{\mathcal{P}}(x, y) = \begin{cases} \Upsilon(x, y) & \text{if } \Upsilon(x, y) > 0, \\ 0 & \text{otherwise,} \end{cases} \tag{B3}$$

and,

$$\Upsilon_{\mathcal{S}}(x, y) = \begin{cases} 0 & \text{if } \Upsilon(x, y) > 0, \\ \Upsilon(x, y) & \text{otherwise.} \end{cases} \tag{B4}$$

Furthermore, the process zones mask may be decomposed in a active and stable process zones mask:

$$\Upsilon_{\mathcal{P}}(x, y) = \underbrace{\Upsilon_{\mathcal{P}}^a(x, y)}_{\text{active}} + \underbrace{\Upsilon_{\mathcal{P}}^s(x, y)}_{\text{stable}} \tag{B5}$$

with,

$$\Upsilon_{\mathcal{P}}^a(x, y) = \begin{cases} \Upsilon_{\mathcal{P}}(x, y) & \text{if } C_{(x,y)}^{\mathcal{K}} \text{ is active,} \\ 0 & \text{otherwise,} \end{cases} \tag{B6}$$

and,

$$\Upsilon_{\mathcal{P}}^s(x, y) = \begin{cases} \Upsilon_{\mathcal{P}}(x, y) & \text{if } C_{(x,y)}^{\mathcal{K}} \text{ is stable,} \\ 0 & \text{otherwise.} \end{cases} \tag{B7}$$

The maximum strain rates added to active and stable cells of the elementary scale are respectively

$$R_{\mathcal{P}}^a = \sum_{x=1}^{\mathcal{L}} \sum_{y=1}^{\mathcal{L}} \Upsilon_{\mathcal{P}}^a(x, y), \tag{B8}$$

and,

$$R_{\mathcal{P}}^s = \sum_{x=1}^{\mathcal{L}} \sum_{y=1}^{\mathcal{L}} \Upsilon_{\mathcal{P}}^s(x, y). \tag{B9}$$

In practice, the shadow zone mask is applied first and $\dot{\varepsilon}(x, y)$ cannot be negative:

$$\Psi_{\mathcal{S}}(x, y) = \max\left(-\dot{\varepsilon}(x, y), \Upsilon_{\mathcal{S}}(x, y)\right), \tag{B10}$$

The amount of strain rate available for the process zone masks is

$$R_{\mathcal{S}} = -\sum_{x=1}^{\mathcal{L}} \sum_{y=1}^{\mathcal{L}} \Psi_{\mathcal{S}}(x, y). \tag{B11}$$

These strain rates may be redistributed by first adding the active process zone mask:

$$\Psi_{\mathcal{P}}^a(x, y) = \Upsilon_{\mathcal{P}}^a(x, y) \left(1 - \max\left(0, \frac{R_{\mathcal{P}}^a - R_{\mathcal{S}}}{R_{\mathcal{P}}^a}\right)\right). \tag{B12}$$

Second, the remaining strain rates

$$R_{\mathcal{S}'} = R_{\mathcal{S}} - \sum_{x=1}^{\mathcal{L}} \sum_{y=1}^{\mathcal{L}} \Psi_{\mathcal{P}}^a(x, y) \tag{B13}$$

are added to the stable process zone mask:

$$\Psi_{\mathcal{P}}^s(x, y) = \Upsilon_{\mathcal{P}}^s(x, y) \left(1 - \max\left(0, \frac{R_{\mathcal{P}}^s - R_{\mathcal{S}}'}{R_{\mathcal{P}}^s}\right)\right). \tag{B14}$$

Then, the remaining strain rates

$$R''_\mathcal{S} = R'_\mathcal{S} - \sum_{x=1}^{\mathcal{L}} \sum_{y=1}^{\mathcal{L}} \Psi^s_\mathcal{P}(x, y) \tag{B15}$$

are finally redistributed uniformly on the fault:

$$\Psi_F(x, y) = \begin{cases} \dfrac{R''_\mathcal{S}}{n_F(\mathcal{K})} & \text{if } C^\mathcal{K}_{(x,y)} \in C^\mathcal{K}_F, \\ 0 & \text{otherwise,} \end{cases} \tag{B16}$$

with $n_F(\mathcal{K})$ the total number of cells of the elementary scale composing the fault F.
Thus the total strain rate redistribution is

$$\Psi(x, y) = \Psi_\mathcal{S}(x, y) + \Psi^a_\mathcal{P}(x, y) + \Psi^s_\mathcal{P}(x, y) + \Psi_F(x, y) \tag{B17}$$